Thermochimica Acta 701 (2021) 178966

Contents lists available at ScienceDirect

Thermochimica Acta

journal homepage: www.elsevier.com/locate/tca

Kinetic analysis of the reduction of a ternary system of Bi, Sb and Te oxides by hydrogen for $BiSbTe_3$ synthesis

Bartosz Trawiński *, Bogusław Kusz

Gdańsk University of Technology, Faculty of Applied Physics and Mathematics, Institute of Nanotechnology and Material Engineering, ul. G. Narutowicza 11/12, 80-233, Gdańsk, Poland

ARTICLE INFO

Keywords:
Reduction in hydrogen
Reaction kinetics
Self-heating
Bismuth antimony telluride

ABSTRACT

Reduction in a hydrogen atmosphere of Bi_2O_3, Sb_2O_3 and TeO_2 mixes oxides for the synthesis of $BiSbTe_3$ was analysed. The reduction reactions of Sb_2O_3 and Sb_2O_4 oxides, as well as Bi_2O_3+Sb_2O_3 and Sb_2O_3+3TeO_2 mixtures, were also evaluated. The reduction of Sb_2O_4 is investigated for the first time. The reactions of the mixed oxides systems also were not the subject of research so far despite being used for synthesis of the $(Bi,Sb)_2Te_3$ material. The study comprised of kinetic analysis of TGA curves performed with non-parametric and iso-conversional methods. Insight into powders' structure during the process was taken to identify processes taking place. The results show, that Sb_2O_3 present in the reduced oxidizes to Sb_2O_4. This redox process between Sb oxide and another oxide takes place directly. The self-heating effect caused by elemental tellurium is diminished in the presence of Bi, because Bi-Te phases decrease the content of the elemental Te.

1. Introduction

Reduction of oxides in a reducing atmosphere, *e.g.* hydrogen in high temperature, is one of the methods of obtaining non-oxide materials. Research of the reduction of different oxide consistently shows that the process occurs at the surface of oxide grains. Simulations of the reduction of nickel oxide show, that surface oxide vacancies play an important role in hydrogen adsorption and dissociation [1]. In the case of iron oxide, the introduction of surface defects and partially amorphous structure through milling resulted in the first step taking place at a lower temperature. The activation energy of that process decreased [2], indicating, that a different mechanism limits the speed of the reaction [3]. A comparison of the previous analysis of the reduction of micrometric and nanometric Bi_2O_3 reduction [4,5] shows, that the reduction process can be performed at a temperature lower by *c.a.* 100 K.

The kinetics of the reduction process in binary and ternary oxide systems has been studied. *E.g.* a study of the reduction of Cu-Fe-Mn and Cu-Fe-Cr oxides [6] shows, that the presence of Mn, compared to Cr, promotes the reduction process. The authors suggest, that this is a result of better adsorption of gaseous reducing agent to the manganese oxide. Nasr et al. [7] studied the synthesis of ferronickel by the reduction of oxides. The powders were pressed into pellets and calcined before the reduction, resulting in a formation of $NiFe_2O_4$. Interestingly, the differing content of Ni not only influenced the reduction process by the formation of the nickel ferrite, but also by changing the porosity of the pellets.

The formation of intermediate oxide products influenced the synthesis of (Ti,W,Mo,V)(CN)–Ni composites by the oxide reduction method [8]. During the reduction of $Cu_5(VO_4)_2(OH)_4$, two separated processes were identified [9]. The first one, comprising the formation of intermediate oxides is controlled by the growth of the nuclei. The second stage is limited by 3D diffusion through a layer of the formed Cu/V_2O_5 composite. These studies show, that the accurate evaluation of such reactions requires not only the analysis of the kinetic data but also the identification of ongoing transformations. A study of the reduction in Fe and Ti oxides system [10] shows, that the elemental reaction and final products of the reduction process can be dependent on the reducing agent (H_2 or CO). In our previous study [5], we showed, that in the Bi_2O_3-TeO_2 system, the reduction process is driven not only by the reactions of individual oxides or their interaction but also by the kinetics of reduction of the emerging double oxides, *i.e.* $Bi_2Te_2O_7$ and $Bi_2Te_4O_{11}$. These results show, that, in the case of complex systems, for a good understanding of the reduction process it is especially important to obtain a proper insight into structural transformations and emerging by-products. Moreover, it is important to find out, how these mechanisms differ between measurements in different thermal conditions. The

* Corresponding author.
E-mail address: bartosz.trawinski@pg.edu.pl (B. Trawiński).

https://doi.org/10.1016/j.tca.2021.178966
Received 12 March 2021; Received in revised form 14 May 2021; Accepted 16 May 2021
Available online 18 May 2021

latter is necessary for the appropriate interpretation of the obtained kinetic analysis results.

In this study, we aim to extend the previous investigation to the reduction process in a ternary Bi, Sb and Te oxides system. This reaction is a way of producing bismuth antimony telluride, a well-known low-temperature p-type material for thermoelectric applications. To provide a better understanding of the process, we will first show the analysis of Sb_2O_3 and Sb_2O_4 antimony oxides reduction. The reduction of Sb_2O_3 oxide was already investigated [11]. However, the process was performed with a mixture of molecular and atomic hydrogen and no detailed kinetic analysis was done. The reduction of Sb_2O_4 has not been investigated so far and the oxide was observed during the reduction in a mixed oxides system. Further, we will discuss phenomena occurring in the Bi_2O_3-Sb_2O_3 and Sb_2O_3-TeO_2 double systems. Data regarding Bi and Te single oxides, as well as their mixture, will be taken from our previous study [5]. Summary of these results together with the recent findings is also provided in Table 1. These results will provide an understanding of the investigated reduction processes. The obtained reduction data and the analysis output are crucial for understanding the reduction of the Bi_2O_3-Sb_2O_3-TeO_2 system. Finally, the ternary system will be analysed in search of relationships between kinetic parameters of the reduction of the mixture ant its constituents.

2. Materials and methods

2.1. Experimental techniques

Bismuth oxide Bi_2O_3 (Acros Organics 99.9 %), antimony oxide Sb_2O_3 (Alfa Aesar 99.9 %) and tellurium oxide TeO_2 (Acros Organics 99+%) were used as raw materials. Sb_2O_4 was synthesized by calcining Sb_2O_3 in the air. Before the reduction process, the oxides used in this study better were milled to decrease temperature and increase the rate of the reduction process. Oxides mixtures were additionally milled to provide good homogeneity. These make the oxide powders more suitable for application in material synthesis by the reduction method. The oxide powders were ball-milled with a Fritsch Pulverisette 7 device in 20 50-minute cycles with 600 rpm rotational speed. Zirconia bowls and zirconia balls with 3 mm diameter were used (ball/powder ratio *ca.* 5:1). Isopropyl alcohol was added to the powders to obtain a narrow dispersion of grains' size and to provide cooling. In the case of mixed oxides, constituents of the mixture were additionally milled in 3 cycles with 150 rpm. SEM microphotographs of the investigated oxide powders and their mixtures after milling are provided in the Supplementary Material, Figs. S1.1-S1.5.

Table 1
Summary of the kinetic analysis.

Reduced material	R^2 in NPK analysis	Kinetic analysis results
Bi_2O_3	0.80	Activation energy initially about 90 kJ/mol, then decreasing to c.a. 40 kJ/mol with diffusional limitation [4,5].
TeO_2	0.88	First-order reaction with E = 69 kJ/mol, strong self-heating effect at 700 K [5].
Sb_2O_3	0.97	Nucleation-growth contolling mechanism with activation energy about 130 kJ/mol, above 830 K data influenced by evaporation of Sb and Sb_2O_3.
Sb_2O_4	0.92	$Sb_2O_4 \rightarrow Sb_2O_3$ – first order with activation energybetween 100 and 130 kJ/mol, further similar to the reduction of Sb_2O_3.
Bi_2O_3+ 3TeO_2	0.80	Bi_2O_3 reduction slowed down in the presence of TeO_2., activation energy 70–90 kJ/mol. For low heating rates formation of $Bi_2Te_4O_{11}$ and $Bi_2Te_2O_7$, and further reduction of these oxides controlling the process above 680 K. Te-related self-heating for high heating rates. Finally, E = 40 kJ/mol and probably diffusional limitation. [5]
Sb_2O_3+ 3TeO_2	0.32	$2Sb_2O_3+TeO_2 \rightarrow 2Sb_2O_4+Te$ reaction at the initial step. Below the temperature of the self-heating, activation energy 130–140 kJ/mol.
Bi_2O_3+ Sb_2O_3	0.64	Almost like separated Bi_2O_3 reduction and Sb_2O_3 reduction. $3Sb_2O_3+Bi_2O_3 \rightarrow 3Sb_2O_4+2Bi$ reaction occurs.
Bi_2O_3+ Sb_2O_3+ 6TeO_2	0.60	Initially reaction controlled by the $Sb_2O_3 \rightarrow Sb_2O_4$ oxidation and reduction of the antimony oxides, after the self-heating process, similarly to the reduction of Bi_2O_3+ 3TeO_2.

The reduction process was performed in our self-build thermogravimetric apparatus, described in a previous paper [4]. Measurements were performed with 2–6 K/min constant heating rates in a hydrogen flow of 160 cm^3/min. The data was recorded every 5 s. The initial mass of the powder samples was about 0.3–0.5 g. Measurements were performed until the measured mass of the sample stopped decreasing or the temperature of 873 K was reached. To determine the structure and composition of samples at different stages of the process, some reactions were interrupted at the selected points. This was achieved by rapid cooling and change of the flowing gas to nitrogen.

The structure of the materials was evaluated with SEM microscopy, using an FEI Quanta FEG 250 microscope with a secondary electrons (SE) detector and a backscattered electrons (BSE) detector. Phase analysis was performed with an XRD technique using Bruker D2 Phaser device with CuK_α (1.542 Å) radiation at room temperature.

2.2. Kinetic data analysis

Firstly, the redaction extent α values were calculated from the obtained TGA data, according to eq. (1) where m_0 is the initial mass of the material, m is the measured mass and m_{ox} is the mass of the oxygen atoms in the starting material.

$$\alpha = \frac{m_0 - m}{m_{ox}} \tag{1}$$

The data were then smoothed using a moving average with a window of 15 points. Next, the time derivative of α was calculated to get the reaction rate r.

The so-obtained derivative data were subject to the kinetic analysis. Kinetics of reactions are based on Eq. (2), where A is a frequency factor, E is the apparent (effective) activation energy, T is temperature, R is the gas constant and f is a function dependent on processes limiting the reaction rate [12]. A, E and f are characteristics of the reaction mechanisms, which may be changing with α and T.

$$r(\alpha, T) = \frac{d\alpha}{dt} = A(\alpha, T) \cdot \exp\left(\frac{-E(\alpha, T)}{RT}\right) \cdot f(\alpha, T) \tag{2}$$

To calculate the dependence of E on α, the Friedman method [13] was used. This method is based on an assumption, that the reaction mechanisms are not dependent on the temperature, at least in the experimental temperature range. Under this condition, eq. (2) can be logarithmized to the Arrhenius-type Eq. (3).

$$\ln r = \frac{-E(\alpha)}{RT} + \ln[A \cdot f(\alpha)] \tag{3}$$

The E value is obtained from the slope of $\ln r$ *vs* $1/T$ dependence in the given α. Several measurements in different thermal conditions are necessary to get the r values at different temperatures for the same given α value. Performing these calculations for different α values results in the $E(\alpha)$ dependence.

Another method used in this study for data evaluation is a non-parametric kinetic (NPK) analysis method based on an assumption, that the reaction rate is a product of independent functions of conversion $f(\alpha)$ and temperature $h(T)$. In the case of independent parallel reaction paths, the equation describing the kinetics has a form of eq. (4), where i denotes different reaction paths.

$$r(\alpha, T) = \sum_i [f_i(\alpha) \cdot h_i(T)] \tag{4}$$

The method belongs to model-free methods, which do not require any assumptions regarding functions describing the investigated process [14]. The method, proposed by Serra et al. [15], is based on singular value decomposition (SVD) of a two-dimensional matrix **R** of the reaction rate r data. Values of matrix elements R_{pq} correspond to $r(\alpha,T)$ experimental data. Let's denote reaction extent and temperature corresponding to coordinates p,q of matrix **R** as α_p and T_q. In our calculations incrementing p values correspond to α values increasing by 0.1 % and incrementing q values correspond to T values increasing by 0.1 K. Matrix **R** is filled with values as follows. All calculated $r(\alpha,T)$ values (from measurements performed in different thermal conditions) are assigned to the nearest p and q coordinates, based on α and T values. If more than one experimental value matches the same matrix coordinates, an average is taken. All R_{pq} matrix elements not determined by the experimental data are interpolated with a cubic interpolation algorithm.

Having the matrix **R** (m × n) constructed, the SVD procedure, described by eq. (5), is performed.

$$R = U \cdot S \cdot V^{T} \tag{5}$$

Matrices **U** and **V** have (m × m) and (n × n) dimensions respectively. Matrix **S** (m × n) is diagonal. Thus, the R_{pq} values can be calculated according to eq. (6), where U, S, V^T and V are elements of matrices **U**, **S**, $\mathbf{V^T}$ and **V**, respectively.

$$R_{pq} = \sum_{i} U_{pi} \cdot S_{ii} \cdot V_{iq}^{T} = \sum_{i} U_{pi} \cdot S_{ii} \cdot V_{qi} \tag{6}$$

Matrices **U** and **V** can be divided into a number of vertical vectors $\mathbf{u_i}$ and $\mathbf{v_i}$ in such a way, that, *e.g.* pth element of vector $\mathbf{u_i}$ (u_{ip}) is equal to the matrix element U_{pi}. The diagonal matrix **S** can be changed into vector **s**, with matrix element S_{ii} equal to vector element s_i. Eq. (6) can be then rewritten to eq. (7).

$$R_{pq} = \sum_{i} u_{ip} \cdot s_i \cdot v_{iq} \tag{7}$$

Comparing eqs. (4) and (7), having in mind, that values R_{pq} correspond to $r(\alpha,T)$, it can be noticed, that vectors $\mathbf{u_i}$ and $\mathbf{v_i}$ correspond to functions $f_i(\alpha)$ and $h_i(T)$ of different reaction paths. Values of vectors $\mathbf{u_i}$ with coordinates p correspond to values of the functions $f_i(\alpha)$ for arguments α_p and values of $\mathbf{v_i}$ with coordinates q correspond to $h_i(T)$ values for arguments T_q. Eq. (8), with an arbitrary real number a_i, is fulfilled.

$$f_i(\alpha_p) = a_i \cdot u_{ip}, \; h_i(T_q) = \frac{s_i}{a_i} \cdot v_{ip} \tag{8}$$

In this study, we only consider the first vectors (i = 1). In SVD, $s_n > s_{n+1}$, so the first vectors are most significant. Moreover, for i>1 both positive and negative values in vectors $\mathbf{u_i}$ and $\mathbf{v_i}$ are present, which is non-physical.

Furthermore, not a whole α-T plane, represented by $\alpha(T)$ plots, is filled with data. Thus, instead of one matrix **R**, several overlapping submatrices **R***j* are analysed (upper index j refers to different submatrices and corresponding vectors and functions). These submatrices are designated in the range covered by the experimental data. To match the results from the analysis of different submatrices, values of a_1^j are chosen to match the condition of eq. (9) and a similar condition for functions h. This allows joining results from the analysis of different parts of the data into functions covering the whole range.

$$f_1^j(\alpha_p) \approx f_1^{j+1}(\alpha_p) \leftrightarrow a_1^j \cdot u_{1p}^j \approx a_1^{j+1} \cdot u_{1p}^{j+1} \tag{9}$$

For each given α, an average of all values of functions $f_1^j(\alpha)$ having the given α in the domain was calculated to get $f_1(\alpha)$ value, and similarly for the $h_1(T)$ function. Having the functions $f_1(\alpha)$ and $h_1(T)$, a correlation of the obtained $r_1(\alpha,T) = f_1(\alpha) \cdot h_1(T)$ with the experimental data was calculated. Only the first set of functions ($i = 1$) is considered in further analysis, therefore a correlation (R^2) of $r_1(\alpha,T)$ with the experimental $r(\alpha,T)$ values is calculated. The R^2 values (average of 5 results, calculated for each heating rate) of reactions investigated in this paper, as well as in the previous work [5], are summarized in Table 1.

3. Results and discussion

3.1. Reduction of antimony oxides

To understand the process of reduction of the constituents of the Bi_2O_3-Sb_2O_3-TeO_2 mixture, the kinetics of Sb_2O_3 was measured. A formation of Sb_2O_4 oxide was observed in the mixed oxides systems, see Figs. S4.5, S5.4, and S6.2 in the Supplementary Material and discussion in further sections. Therefore the reduction of this compound was also investigated. The measured $\alpha(T)$ dependencies are presented in the Supplementary Material, Figs. S2.1 and S3.1. The reaction rate dependence on the temperature is presented in Fig. 1 for both oxides. To provide comparability of the Sb_2O_3 reduction data and the $Sb_2O_3 \rightarrow Sb$ part of the Sb_2O_4 reduction, the reaction rate values of the Sb_2O_4 reduction were multiplied by 4/3. The reduction of Sb_2O_4 consists of two processes, the second of which well agrees with the reduction of Sb_2O_3.

XRD analysis of the phase composition (diffraction pattern available in Supplementary Material, Fig. S3.3) shows, that the initial part of the reduction of Sb_2O_4 results in the formation of Sb_2O_3. A small amount of elemental antimony was also identified in the material. The $r(\alpha)$ dependences, provided in Fig. S3.2 confirm, that the first part of the reaction corresponds to 25 % conversion. Fig. 1 shows, that the reaction further progresses similarly to the Sb_2O_3 reduction. The only difference is the results obtained with the 2 K/min heating rate, above 810 K, where the Sb_2O_4 reduction process is faster than the Sb_2O_3 reaction.

Fig. 2 shows a comparison of Sb_2O_3 and Sb_2O_4 powders as-prepared for the reduction process and heated in hydrogen until the Sb_2O_3 reduction starts (780 K). Notice, that the initial Sb_2O_3 powder (Fig. 2a) is non-monodisperse. Grains with hundreds of nanometres in size are covered by smaller (below 50 nm) ones. Upon heating to the onset of the reduction, the size increases and the smaller grains disappear (Fig. 2b). A more homogenous powder results from the milling of Sb_2O_4 (Fig. 2c). During the reduction to Sb_2O_3, large (20−30 μm) particles are formed (Fig. 2d). Bipyramidal symmetry of these particles suggest, that these are crystalline particles. However, an unusual structure of these grains is observed with holes visible on the surface and inside the grains. The holes are filled with nanostructured material, which is also present on the surface of the large grains.

Chernogorenko et al. [11] shown, that the reduction of Sb_2O_3 is interfered with by the evaporation of the obtained antimony. For this reason, the presented herein Sb_2O_3 oxide reduction with the 2 K/min heating rate up to 840 K resulted in over 150 % of the expected mass change. Fig. S2.2 shows the diffraction pattern of as-obtained material, indicating, that the reduction process is not completed. In the reaction of Sb_2O_4 (Fig. 1), mass changes stopped for low heating rates, reaching over 120 % of the expected value in the case of the 3 K/min rate and over 150 % for 2 K/min.

The non-parametric kinetic analysis of the Sb_2O_3 oxide reduction with hydrogen was performed. For, this reaction, the highest correlation coefficient of all processes was obtained, see Table 1. The calculated $h(T)$ function is presented in Fig. 3 in the Arrhenius coordinates. The calculated function is linear between 790 and 830 K. Therefore, in this temperature range, the reaction has an activation behaviour with activation energy equal to 129 kJ/mol. In lower temperatures, the deviation from the linear behaviour can be related to a higher noise/signal ratio lower reaction rate. Noticeably, above 830 K the submatrices cannot be matched using the eq. (9) to form a function. This indicates, that above 830 K the assumption is given in eq. (4) is not fulfilled. Consequently, the 186 kJ/mol energy value, given for orientation only, should not be considered as describing the reaction.

The obtained f function, presented in Fig. 4 also shows a change in the reaction progress since the 11th submatrix. Before this, the reaction tends to reach about 100 % conversion. The function, calculated from

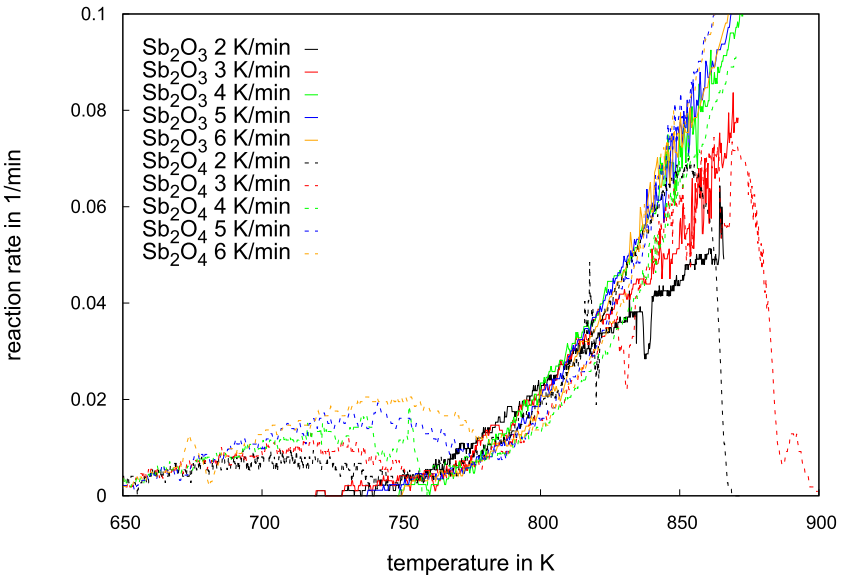

Fig. 1. Dependence of the reaction rate of the temperature during the reduction of Sb_2O_3 and Sb_2O_4 (multiplied by 4/3).

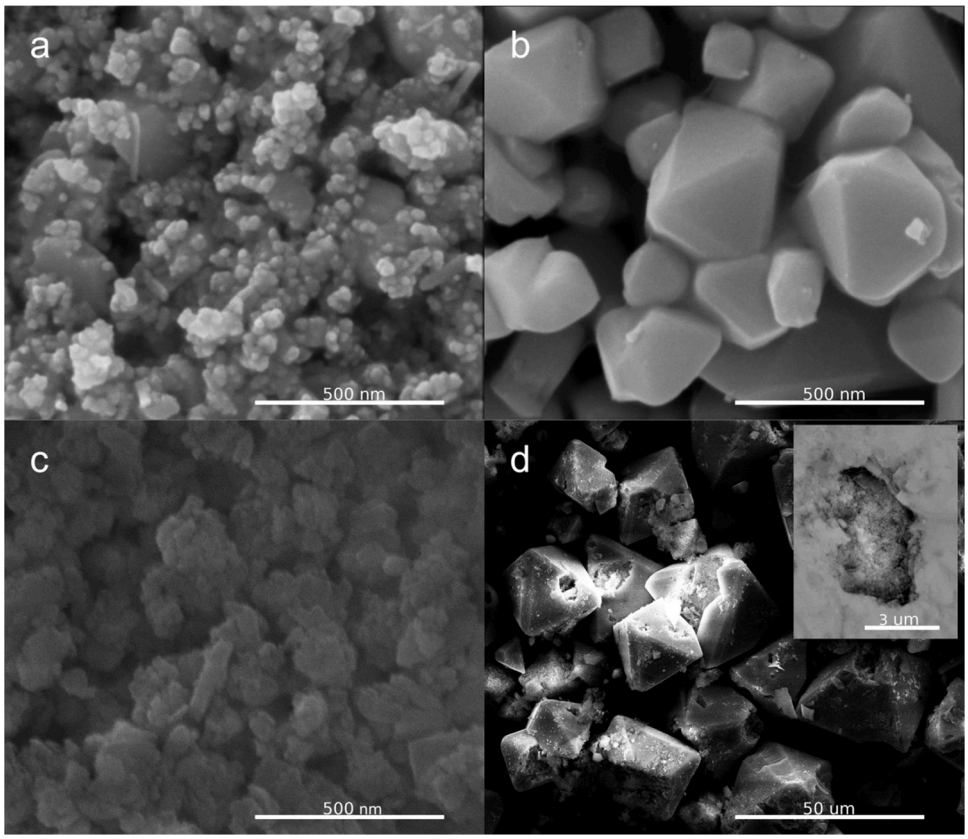

Fig. 2. SEM images (SE detector) of a) Sb_2O_3 powder, b) Sb_2O_3 heated up to 780 K in hydrogen with 2 K/min heating rate, c) Sb_2O_4 powder, d) Sb_2O_3 obtained from Sb_2O_4 by the reduction in hydrogen up to 780 K with 2 K/min heating rate; inset in panel d shows a cross-section view of a large grain with a hole filled with nanoparticles.

submatrices 1–10 (with an average taken in the regions of overlapping), was fit to a Šesták-Berggren (SB) equation in the form of eq. (10) [16] with a scaling factor b, matching the equation to the calculated values.

$$f(\alpha) = b\alpha^n(1-\alpha)^m \tag{10}$$

The obtained values of fit parameters are: $b = 0.13$, $n = 0.34$, $m = 0.81$. SB functions with different m, n parameters similar to different reaction models. For $m = 0.806$ and $n = 0.515$, the dependence is similar to the 2nd order Avrami-Erofeev nucleation-growth model [17]. Among different solid-state reaction models [18], reaching a maximal value for a specific α (not 0 or 1) is characteristic of nucleation-growth models. It is worth noting, that these models describe microscopic transformations of the solid-state, rather than chemical reactions on a molecular scale [19]. Above 830 K (or 10th submatrix), the tendencies change. The

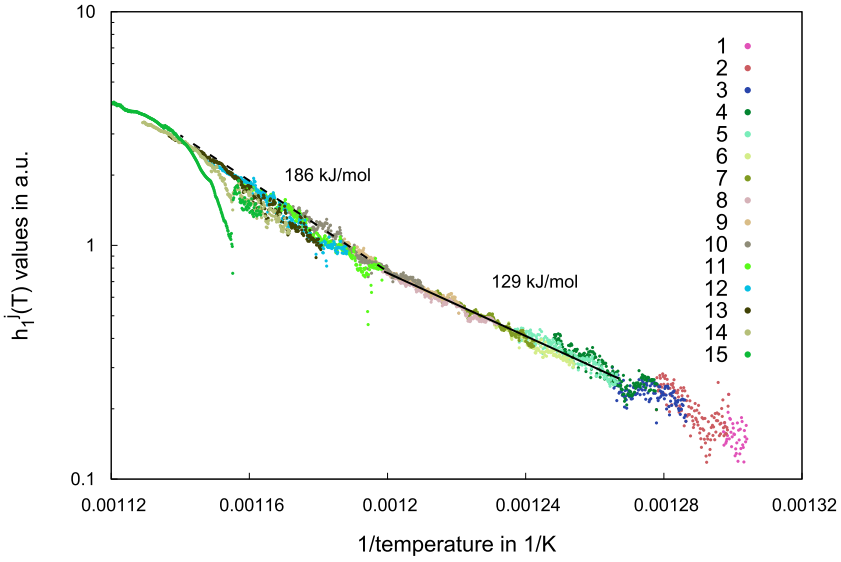

Fig. 3. Thermal function $h(T)$ calculated with the NPK analysis of the reduction of Sb_2O_3. Values in the key stand for j indices of vectors $\mathbf{v_1}j$. The dashed line and the corresponding E value is for orientation only.

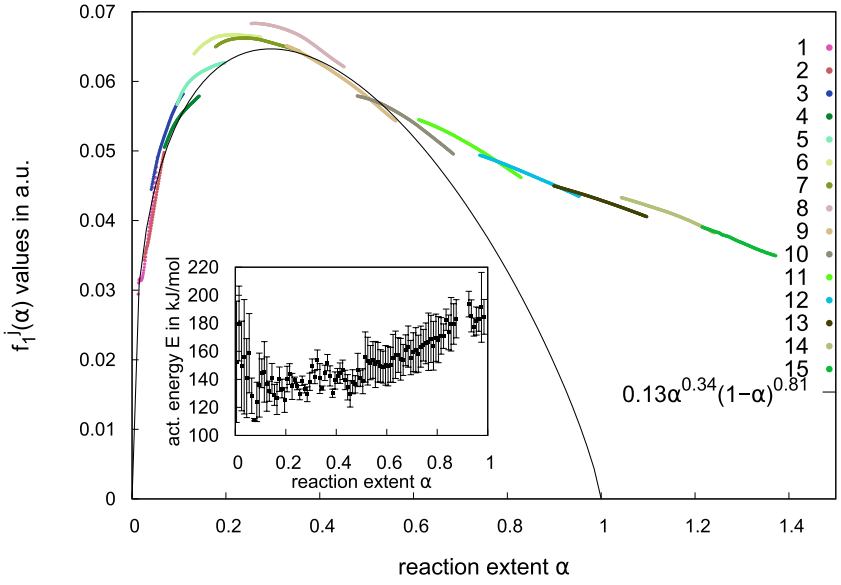

Fig. 4. Conversion function $f(\alpha)$ calculated with the NPK analysis of the reduction of Sb_2O_3. Values in the key stand for j indices of vectors $\mathbf{u_1}j$. Inset: dependence of the activation energy on the reaction extent calculated with the Friedman method.

conversion function (Fig. 4) increases relative to the first region, fitted with the SB function. We match this to evaporation. Thus, it can be concluded, that the volatility becomes significant above 830 K. This is consistent with thermodynamic predictions [20], indicating, that the antimony oxide begins to volatilize in about 820 K.

The results of the Friedman analysis are in an agreement with the NPK results, in the range of 6–50 % of the reaction extent. The isoconversional analysis returned higher values (137 kJ/mol on average), however, in the range of uncertainties, the NPK value of 129 kJ/mol fits the results.

Comparison of the TG curves obtained in an inert atmosphere by Karlsson et al. [20] shows similarity with the reduction results. Thus, the process of Sb_2O_3 reduction investigated herein is not dependent (or entirely dependent) on the reaction of the oxide with hydrogen.

Similarly, the kinetics of the reduction of Sb_2O_4 were evaluated. The obtained $\mathbf{u_1}j$ vectors, presented in Fig. 5, can be matched up to 25 % of the reaction extent, corresponding to the formation of Sb_2O_3. Besides initial fluctuations, a linear dependence is observed. Therefore, the reaction can be described by a first-order reaction model. In contrast to the Sb_2O_3 reduction discussed above, the reaction of antimony(III) oxide obtained from Sb_2O_4 cannot be analysed by the NPK – the calculated vectors $\mathbf{u}$ do not match each other, see inset in Fig. 5.

Isoconversional analysis of the activation energy, presented in Fig. 6, shows, that the energy barrier, averaged in the range of 0–22 %, is equal to 105 kJ/mol. This value is lower than 121 kJ/mol, calculated from the NPK results, provided in Fig. S3.4. Above 10 % of the reaction extent, the NPK value agrees with the isoconversional analysis results within the uncertainty limit. Moreover, the range of the activation energy calculation from the $h(T)$ function is narrow. Additionally, there are deviations from linearity, introducing uncertainty of 10 kJ/mol. For further stages of the reduction of Sb_2O_4, which is in fact the reduction of Sb_2O_3, the activation energy values are slightly higher from the value found for the Sb_2O_3 reaction (*c.a.* 130 kJ/mol, inset in Fig. 4), value. However, within the uncertainty margins, the values are in agreement.

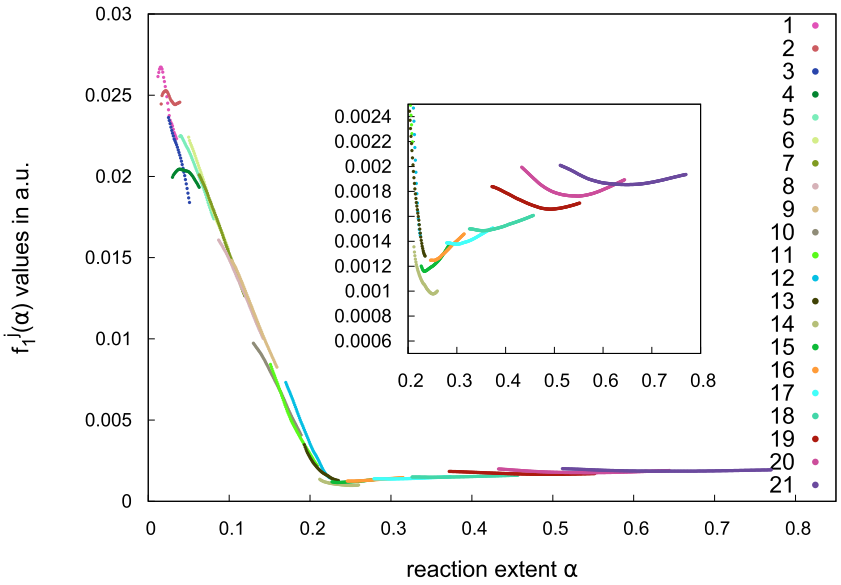

Fig. 5. Conversion function $f(\alpha)$ calculated with the NPK analysis of the reduction of Sb_2O_4. Values in the key stand for j indices of vectors $\mathbf{u}_1 j$.

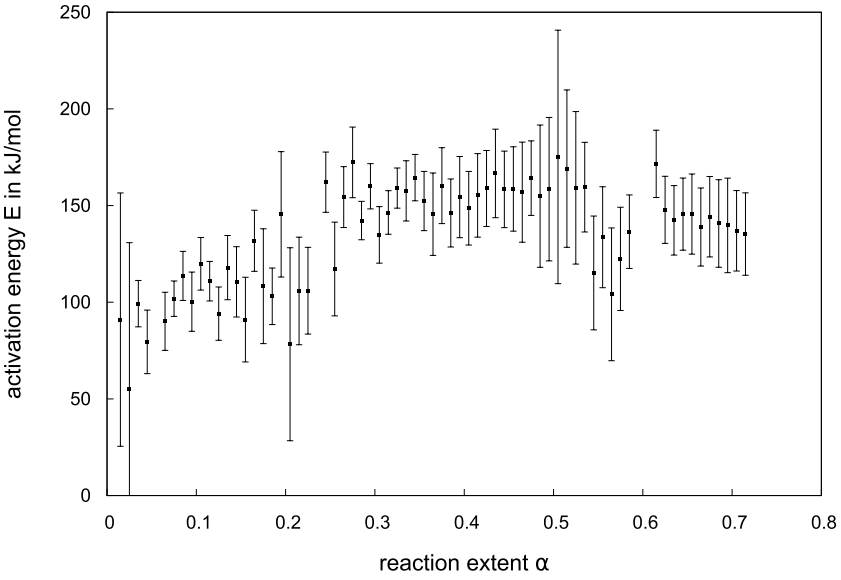

Fig. 6. Dependence of the activation energy of the Sb_2O_4 reduction on the reaction extent, calculated with the Friedman method.

Moreover, the increase of the activation energy observed for the Sb_2O_3 reduction at the end of the process is not found.

3.2. *Reactions in the antimony oxide – tellurium oxide system*

The reduction of the Sb_2O_3+3TeO_2 system was studied with the stoichiometry corresponding to the synthesis of Sb_2Te_3, belonging to the $(Bi,Sb)_2Te_3$ system investigated herein. The measured reaction rate dependence on temperature and the differential $r(T)$ data is provided in the Supplementary Material, Figs. S4.1 and S4.2. Fig. 7 shows a comparison of the differential data obtained during the reduction of single and mixed oxides with the 4 K/min heating rate, which is also representative of the other rates. The TeO_2 values were multiplied by 2/3 and these of Sb_2O_3 by 1/3 to match the ratio of the oxygen content in these oxides to the overall content in the mixed oxides. The Sb_2O_4 data was additionally multiplied by 4/9 (see explanation below).

Noticeably, the change in the sample's mass starts in the temperature similar to the beginning of the Sb_2O_4 reduction. Indeed, a presence of the Sb_2O_4 oxide after heating up to 590 K was confirmed. XRD phase analysis of the material heated with a 2 K/min rate in nitrogen and hydrogen atmospheres (Figs. S4.3 and S4.4) show a small content of the antimony(III,V) oxide. The elemental tellurium was not identified, however, it could be below the detection limit. It has been shown [21], that the tellurium oxide does not thermally decompose in experimental conditions. Consequently, there are no any oxide particles that would oxidize the antimony oxide. Therefore, a direct $2Sb_2O_3+TeO_2 \rightarrow 2Sb_2O_4+Te$ reaction takes place. The reaction of TeO_2 with hydrogen below 590 K cannot be ruled out. In such a case the emerging water would oxidize the antimony oxide: $2Sb_2O_3+H_2O \rightarrow 2Sb_2O_4+H_2$. The similarity of the XRD results of powders obtained with the two different atmospheres indicates, that the direct redox process between oxides is comparable or even faster than the reaction with H_2 and H_2O intermediates. At 690 K, antimony is found only in the form of Sb_2O_4 (see X-Ray pattern Fig. S4.5). The mixed antimony and tellurium oxides powder treated up to a similar temperature in nitrogen also contain no Sb_2O_3, however, evaluation of the

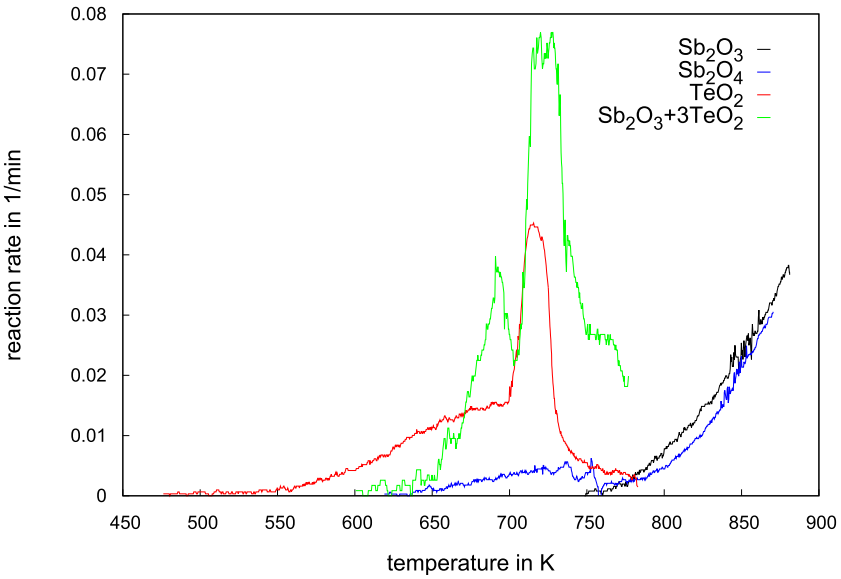

Fig. 7. Dependence of the reaction rate of the temperature during the reduction of Sb_2O_3+3TeO_2 mixed oxides and corresponding single oxides. Data for Sb_2O_3 is multiplied by 1/3, TeO_2 by 2/3 and Sb_2O_4 by 4/9.

diffraction result, Fig. S4.6, is difficult. In the latter experiment, no changes in mass were observed. Having these observations in mind we can conclude, that the reduction of the tellurium oxide follows two parallel paths. One is a direct reduction with hydrogen $2H_2+TeO_2 \rightarrow Te+2H_2O$. The second path comprises $2Sb_2O_3+TeO_2 \rightarrow 2Sb_2O_4+Te$ reaction between grains and the reduction of the antimony(III,V) oxide $2Sb_2O_4+H_2 \rightarrow 2Sb_2O_3+H_2O$. The latter pathway may also comprise of reduction of TeO_2 with hydrogen and oxidation of Sb_2O_4 with emerging water. Interestingly, the oxidation of Sb_2O_3 (in its cubic Senarmontite form) in the investigated system takes place in lower temperatures than in the case of oxidation in air, which begins around 800 K [22].

The correlation coefficient of the non-parametric analysis results with the experimental data, equal to 0.32, is lowest for the reduction of mixed Sb_2O_3+3TeO_2 oxides. The NPK results underestimate the reaction rate. This may results from considering only one set of *f* and *h* functions. However, the further $\mathbf{u_2}$ and $\mathbf{v_2}$ vectors are disordered and changing between positive and negative values, see exemplary results in Figs. S4.7 and S4.8. Consequently, the analysis results should be considered cautiously. However, the results are in agreement with some expectations, *e.g.* in the investigated process, a self-heating process above 700 K can be identified. Similarly to previous results for the reduction of Bi_2O_3+3TeO_2, this effect manifests itself with rapidly increasing *h*(*T*) function above 700 K, see Fig. 8. Thus, the NPK results shouldn't be completely neglected. Locally increased temperature causes a faster reduction of the antimony oxides. Indeed, at 750 K, when pure Sb_2O_3 undergoes reduction, the reaction progress exceeds 2/3 corresponding to the fraction of oxide in TeO_2. Apparent activation energies were calculated for linear parts of the function. In the low-temperature range, the calculations were also performed, returning 388 and 258 kJ/mol. These values seem to be unreasonably high.

The activation energies presented in Fig. 8 are close to those found for the reduction of antimony oxides (in the range of 100−150 kJ/mol). These values are also consistent with the isoconversional analysis results below the self-heating temperature (Fig. 13), and differ from these of TeO_2 (*c.a.* 70 kJ/mol).

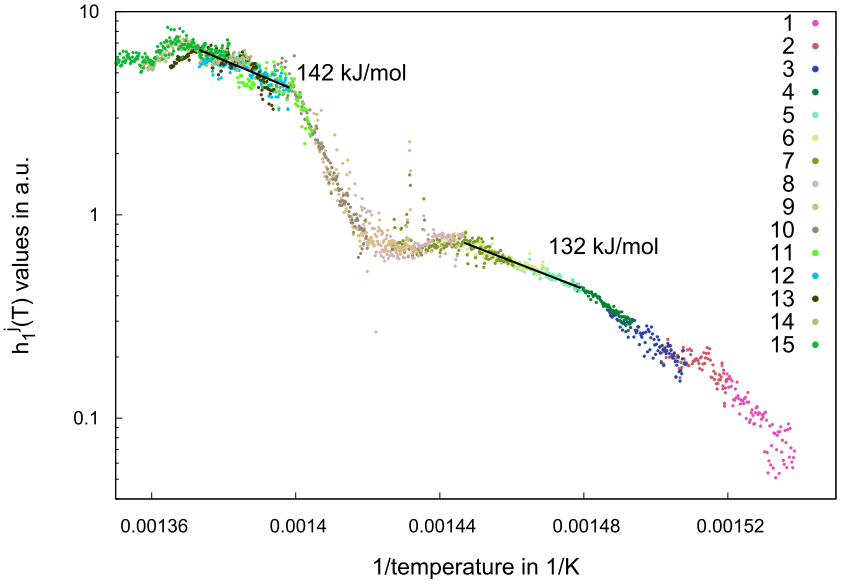

Fig. 8. Thermal function *h*(*T*) calculated with the NPK analysis of the reduction of Sb_2O_3+3TeO_2. Values in the key stand for j indices of vectors $\mathbf{v_1}j$.

3.3. Reactions in the bismuth oxide – antimony oxide system

Furthermore, a reduction of the Bi_2O_3+Sb_2O_3 mixed oxides was investigated. The measured $\alpha(T)$ dependencies as well as differentiated data plots are provided in the Supplementary Material, Figs. S5.1-S5.3. Fig. 9 shows a comparison of the $r(T)$ dependence in the experiment with a 4 K/min heating rate, compared with corresponding results for the single oxides. The comparison is representative for all applied heating rates, however, for higher rates, the two processes are overlapping (see Figs. S5.2 and S5.3).

The reduction of the mixed oxides consists of two separated reactions. The first one is related to the Bi_2O_3+$3H_2$→$2Bi$+$3H_2O$ process. An enhancement of the reaction rate is visible close to the initiation of the reduction of Sb_2O_4. This suggests, that a $3Sb_2O_3$+Bi_2O_3→$3Sb_2O_4$+$2Bi$ reaction and further $2Sb_2O_4$+H_2→$2Sb_2O_3$+H_2O reduction take place. Indeed, XRD evaluation of the partially reduced sample shows, that in the temperature of 590 K (Fig S5.4) the material comprises metallic bismuth, bismuth oxide, antimony(III,V) oxide and traces of antimony(III) oxide. XRD phase analysis (Fig. S5.5) reveals Bi + Sb_2O_3 composition after the first step, therefore, the first stage is effectively a Bi_2O_3 reduction (with the Sb_2O_4 by-product, which is reduced to Sb_2O_3). The first part of the process should therefore correspond to 50 % of the expected mass change. However, measurements show about 2/3 of the expected conversion. Bismuth and antimony form a system with unlimited solubility [23]. Consequently, only one phase is identified in the diffraction pattern of the material after completion of the reduction process (Fig. S5.6).

The reduction of bismuth and antimony are parallel and partially overlapping – the reduction of Sb_2O_4 and Bi_2O_3 occurs at the same time. Additionaly, in the case of 5 and 6 K/min heating rates, the steps comprising Bi_2O_3 and Sb_2O_3 reduction are not separated. Having this in mind, one would expect the presence of at least two processes separated by the non-parametric method in these submatrices j, which cover the reduction of both oxides. Notwithstanding, for i>1 vectors, non-physical results were obtained, as described in Section 2. Nevertheless, the constructed function $f(\alpha)$, plotted in Fig. 10, shows separation into two parts, which, similarly to the Sb_2O_3 reduction, show increasing and then decreasing characteristic.

The calculated dependence of the activation energy on the progress of the process is in agreement with the identified steps. Initially, the value of *c.a.* 80 kJ/mol fits the initial value during the reduction of Bi_2O_3 powder – see [4,5,24]. 50 kJ/mol between 20 and 45 % of the conversion is equal to the value found at the end of the reduction of Bi_2O_3. However, the latter value was identified with the Friedman method only at the very end (α>0.8) of the Bi_2O_3 reduction process. The 80 kJ/mol occurring above 50 % is between the value for Bi_2O_3 and that of Sb_2O_4 reduction to Sb_2O_3 (100 kJ/mol). This is the expected result for parallel reactions, for which the effective activation energy is a weighted average with coefficients equal to the contributions to the total reaction rate [25].

Noticeably, the reduction of antimony oxide is enhanced in the presence of metallic bismuth. The process is much faster at low temperatures. A completion is achieved below 830 K, preventing the evaporation of antimony. According to the Bi-Sb phase diagram [26], the 1:1 Bi:Sb mixture is completely in the liquid phase at 770 K. Consequently, at the end of the measured reduction processes, the material is melted. Only in the 2 K/min measurement 15 at.% of the material is in solid-state. After the TGA measurements, the materials were cooled rapidly. The obtained powder had spherical particles. The elemental composition measured with EDX was 2:1 Bi:Sb on the surface. Analysis of the cross-section, Fig. S5.7 in the Supplementary Material, revealed a composition close to 1:1 inside grains. No traces of oxide phases were identified.

3.4. Synthesis of $BiSbTe_3$

The reduction of mixed bismuth, antimony and tellurium oxides, leading to the formation of $(Bi,Sb)_2Te_3$ was investigated. TGA results are presented in Supplementary Material, Fig. S6.1. Analysis of the dependence of the reaction rate on temperature is presented in Fig. 11. Several processes can be identified. The first one initiates similarly for each heating rate. Maximum of the rate of the first process is increasing with increasing rate, typically for non-isothermal reactions. Further, a second maximum of the reaction rate can be identified for each run. However, this maximum is related with different reactions for different heating rates, which is indicated by different onset temperatures – 700 K in the case of the 2 K/min measurement and 730 for the 6 K/min one. The next process can be identified for 3, 4 and 5 K/min heating rates, manifesting itself by slowly decreasing the reaction rate above 760 K. The last process is visible above 860 K.

The observed mass changes initiate similarly to the Sb_2O_3+$3TeO_2$ mixed oxides reduction, which is also indicated by similar initial results

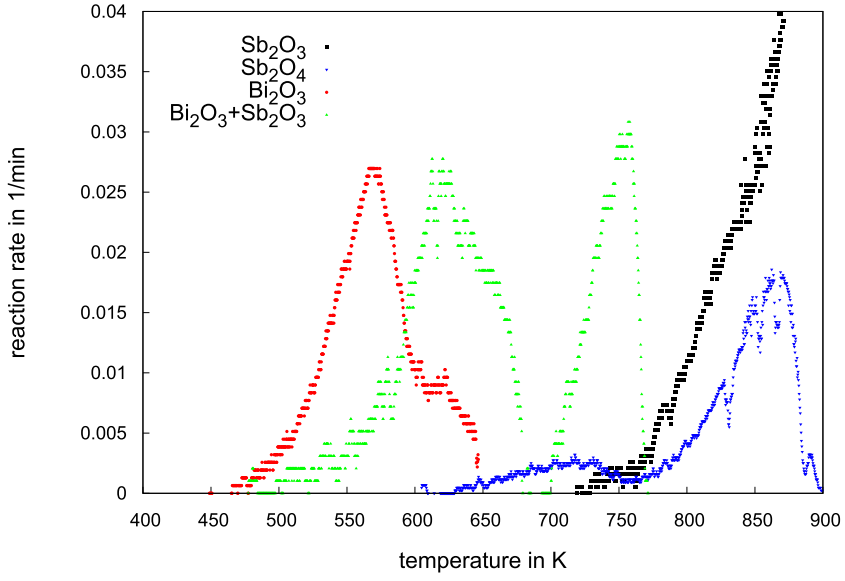

Fig. 9. Dependence of the reaction rate of the temperature during the reduction of Bi_2O_3+ Sb_2O_3 mixed oxides and corresponding single oxides with 4 K/min heating rate. Data for Bi_2O_3 and Sb_2O_3 is multiplied by 1/2, Sb_2O_4 by 1/3.

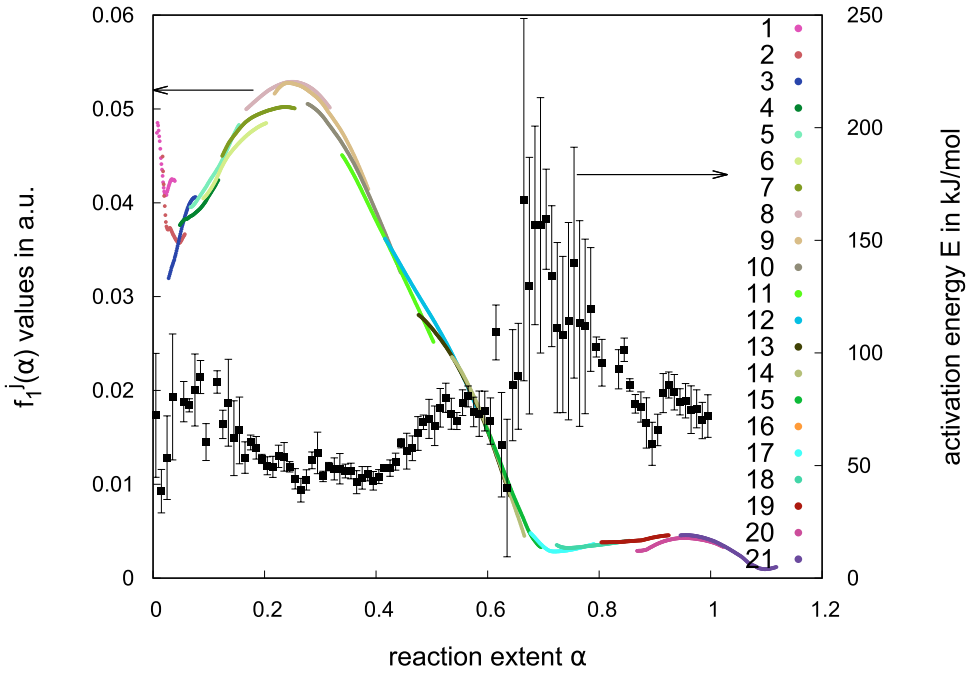

Fig. 10. Conversion function $f(\alpha)$ calculated with the NPK analysis of the reduction of Sb_2O_3+ Bi_2O_3. Values in the key stand for j indices of vectors $\mathbf{u_1}j$; activation energy values calculated with the Friedman method.

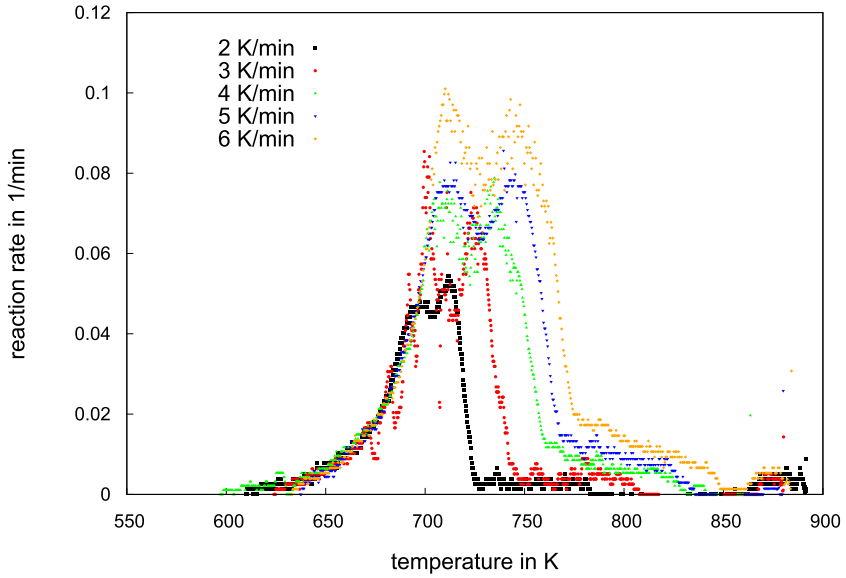

Fig. 11. Dependence of the reaction rate of the temperature during the reduction of Bi_2O_3+Sb_2O_3+6TeO_2.

of the non-parametric analysis. The calculated conversion functions are presented in Fig. 12. In both systems, values of the function are nearly constant (despite initial fluctuations, which can be neglected due to high inaccuracy). Notice, that the mixed bismuth and tellurium oxides are reduced from 530 K (with 4 K/min rate) [5]. Again, the delay results from oxidation of Sb_2O_3 to Sb_2O_4. This is confirmed by the presence of Sb_2O_4, elemental Bi and Te in the material heated up to 620 K (in a hydrogen atmosphere, 3 K/min), confirmed by an XRD pattern, Supplementary Fig. S6.2. At 663 K the material consists of the same phases, see Fig. S6.3.

Sample reduced with a 2 K/min heating rate up to 700 K, at which the second maximum of the reaction rate starts, was analysed with XRD. The pattern (Fig. S6.4) shows, that the sample consists mainly of $BiSbTe_3$, Te and traces of $BiTe_2$. The temperature matches the temperature of the Te-related self-heating effect. Oxides are undetectable for X-ray diffraction. However, when a higher heating rate (4 K/min) is applied, the two antimony oxides can be identified at 720 K, see Fig. S6.5. Noticeably, Sb_2O_3 was found in a metastable valentinite structure. Previously, a metastable structure of tungsten was obtained by the reduction of WO_3 [27]. Metastable suboxides were also found during the reduction of MoO_3 [28]. The presence of antimony oxide explains the higher onset temperature of the second maximum of the reaction rate, which agrees with the initiation of the Sb_2O_3 reduction. Notice, that for higher heating rates, the shift of the reaction rate $r(T)$ dependence towards higher temperatures is generally expected. Therefore, the evaluation of the phase composition was crucial for the identification of the change of the mechanism related to the second maximum and appropriate interpretation of the kinetic data. Interestingly, in the

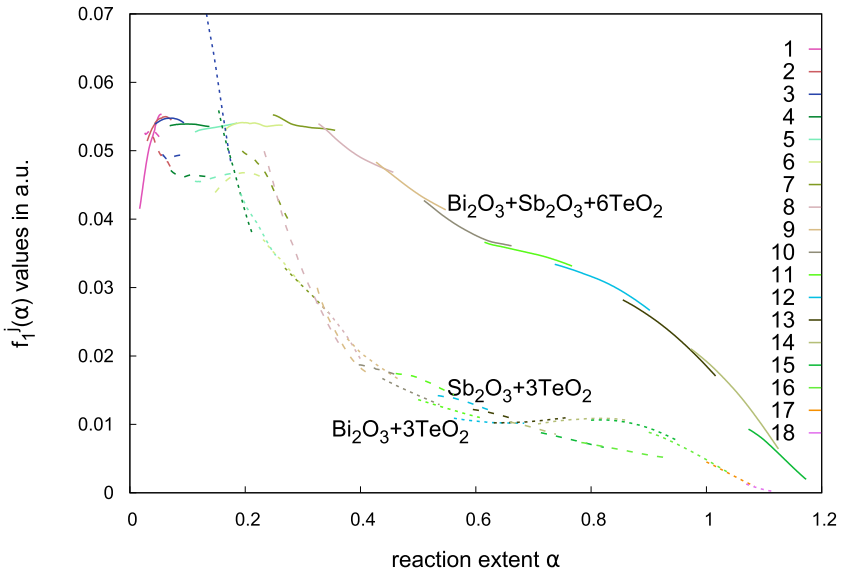

Fig. 12. Conversion function $f(\alpha)$ calculated with the NPK analysis of the reduction of Bi_2O_3+$3TeO_2$ (dotted line), Sb_2O_3+$3TeO_2$ (dashed line) and Bi_2O_3+Sb_2O_3+$6TeO_2$ (solid line). Values in the key stand for j indices of vectors $\mathbf{u}_1 j$.

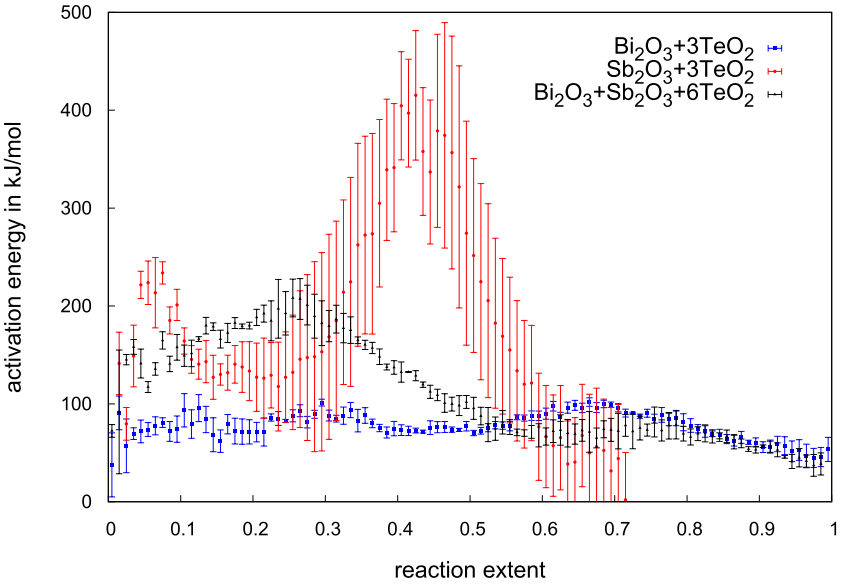

Fig. 13. Dependence of the activation energy on the reaction extent during the reduction of Bi_2O_3+$3TeO_2$ (previous work [5]), Sb_2O_3+$3TeO_2$ and Bi_2O_3+Sb_2O_3+$6TeO_2$, calculated with the Friedman method.

three-oxide system, the self-heating effect is not as pronounced as in other investigated processes involving the tellurium oxide. The results of the isoconversional analysis, presented in Fig. 13, show only a small (compared to that on the Sb_2O_3+$3TeO_2$ curve) upturn starting from α = 0.2, corresponding to 700 K in the 6 K/min run. The large activation energy maximum for the Sb_2O_3+$3TeO_2$ mixture, starting above 20 % conversion, is a result of the self-heating effect, similarly to previously found for the TeO_2 reduction [5]. Before the maximum, the E values match to that calculated with the NPK method (Fig. 8). These values match to the reduction of antimony oxides. The non-parametric analysis (Fig. S6.6 in the Supplementary Material) does not show any trace of self-heating in the three oxides system.

Considering also the previous results regarding the reduction of the Bi_2O_3+TeO_2 mixture [5], we can conclude, that the self-heating effect occurring at 700 K, related to elemental tellurium is suppressed when Bi is present. In the Bi_2O_3+$3TeO_2$ and Bi_2O_3+Sb_2O_3+$6TeO_2$ systems the increase of the reaction rate at 700 K is relatively smaller than in the reduction of TeO_2 and Sb_2O_3+$3TeO_2$, see Fig. S6.8 in the Supplementary Material. In the case of the Bi-containing powders, there is no significant change of the thermal dependencies of activation energy or the thermal function h. It should be emphasized, that in the case of self-heating, these observed changes result from the actual local temperature being higher than the measured values. Notice, that in the samples with Bi, elemental Te is not detected by XRD close to 700 K. The reduced tellurium forms intermetallic phases with the reduced bismuth. Consequently, the Te-related effect does not occur or is too weak to significantly increase the local temperature and cause disturbances in the kinetic analysis results.

In contrast to the initial part of the reduction of the three mixed oxides, the final stage shows similarity to the reduction of mixed bismuth and tellurium oxides, indicated by the similar output of the analysis in the reaction extent domain – conversion function form NPK

and activation energy from isoconversional analysis. Between *c.a.* 30 % and 60 % conversion the function *f* is decreasing nearly linearly. Above 60 %, the function is concave, however, a local maximum is not observed. Fig. S6.7 shows a comparison between scaled conversions functions resulting from the NPK analysis of the two reduction processes.

The microstructure of the powder at different stages of the process was evaluated. SEM imaging of powder cross-sections in the BSE mode and EDX elemental analysis were used. Images are presented in Fig. 14. Different phases are visible with different intensities. Fig. 14a and b show the oxide mixture processed with the 3 K/min rate up to 620 and 663 K respectively. The material remains nanostructured, agglomerating grains have diameters below 100 nm. The phase-contrast images show the presence of outstanding bright areas. The elemental analysis of these areas shows increased content of Te, especially for the higher temperature. In the BSE imaging brightness is related to the atomic number [29]. Therefore, in these areas, the content of the reduced material (without light oxide atoms) is higher than the average.

Fig. 14c shows the material reduced up to 700 K with a 2 K/min heating rate. BSE image shows a multi-phase structure of the powder. Bright areas consist of the $(Bi,Sb)_2Te_3$ phase. In the marked grey areas, a significant amount of oxide is present. Fig. 14d shows the material reduced up to 756 K with a 4 K/min heating rate. At this stage, the powder consists mainly of a phase with a composition close to $BiSbTe_3$, with Sb deficiency in relation to Bi. Embedded Te-rich areas are also visible. The identification of other elements in these areas can be a result of the low spatial resolution of the EDX method. The shape of these areas results from filling the available voids with liquid Te. No oxide phases were identified by XRD, however, at this stage, the reduction is not completed. Considering Sb deficiency in the $BiSbTe_3$ and presence of elemental tellurium, the presence of antimony oxide is possible XRD result shows only the $BiSbTe_3$. Additional phases are embedded in the $BiSbTe_3$ and therefore are undetectable in the diffraction pattern. Notice, that the $(Bi,Sb)_2Te_3$ phase was not identified with XRD in the materials presented in panels a and b, diffraction patterns are given in Figs. S6.2 and S6.3. This confirms, that the most significant growth of the grains is related to the formation of the bismuth antimony telluride phase.

Finally, the elemental composition and homogeneity of the obtained $BiSbTe_3$ material was evaluated with EDX mapping. Fig. 15 shows a view of a cross-section of the obtained powder. The visible grain can actually be an agglomerate of crystallites. Intensity maps of the relevant elements are provided. Noticeably, the composition is uniform across the whole area. The overall ratio of the elements Bi:Sb:Te is equal to 1:1:3.

4. Conclusions

The reduction of a mixture of bismuth, antimony and tellurium oxides in hydrogen, leading to the formation of the $BiSbTe_3$ phase was investigated. Kinetic analysis based on the thermogravimetric analysis in non-isothermal conditions was performed. Microstructural transformations were investigated. For a better understanding of the process, the reduction of antimony oxides, as well as a mixture of antimony and tellurium oxides, were evaluated.

The research has shown, that the Sb_2O_4 oxide undergoes reduction to Sb_2O_3. This reaction starts at the temperature of about 650 K. The non-parametric kinetic analysis shows, that the reaction can be described as first-order (with respect to Sb_2O_4) with activation energy 131 kJ/mol. The isoconversional method returned a lower value (105 kJ/mol) of the latter parameter. The reduction of Sb_2O_3 in hydrogen can be described by a nucleation-growth mechanism with activation energy close to 130 kJ/mol. Above 830 K significant evaporation of the oxide and elemental antimony occurs. Despite the difference in microstructure, Sb_2O_3

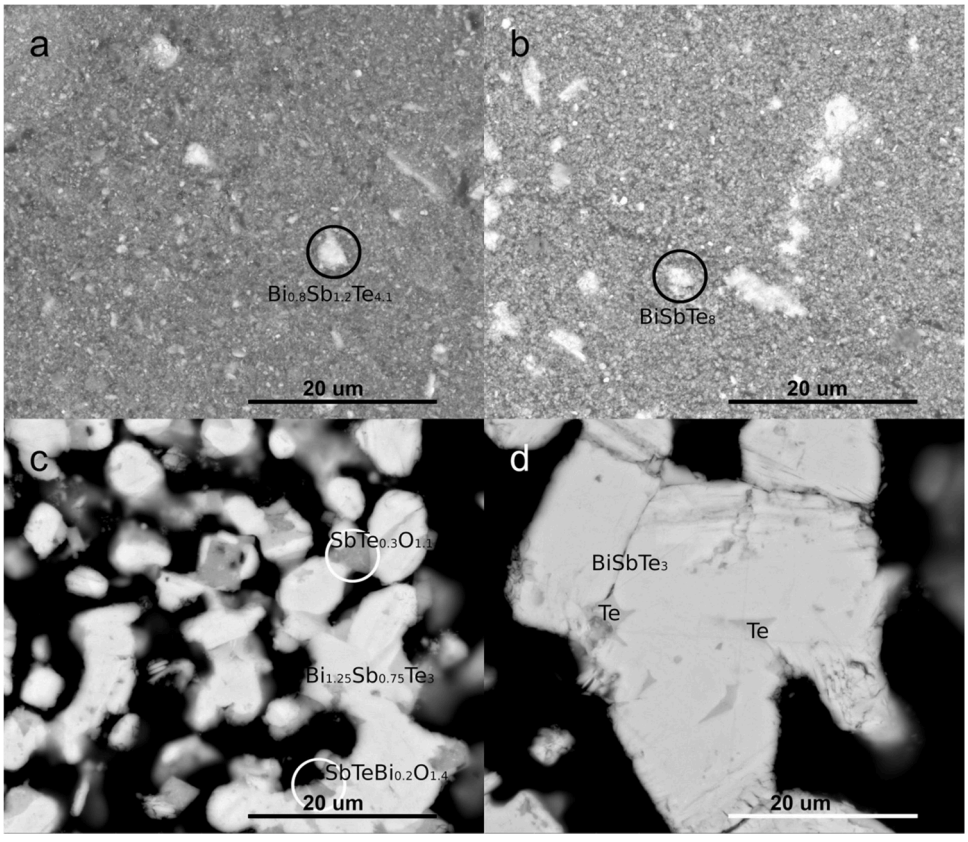

Fig. 14. SEM images (BSE detector) of Bi_2O_3+Sb_2O_3+6TeO_2 powder reduced a) up to 620 K, b) up to 663 K with 3 K/min rate, and c) up to 700 K with 2 K/min rate with approximate compositions measured in particular places, d) up to 756 K with 4 K/min rate with identified phases.

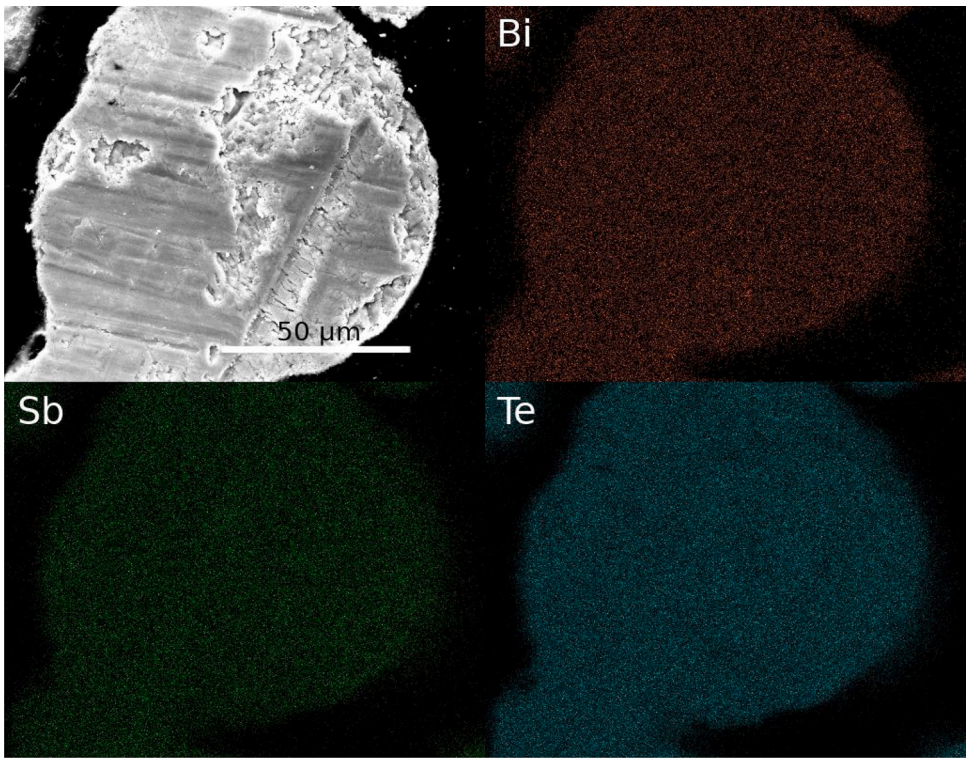

Fig. 15. SEM images (SE detector) of a cross-section of $BiSbTe_3$ powder obtained by reduction of oxides with the 4 K/min heating rate and maps of the intensities of signals of different elements obtained with EDX.

resulting from the reduction of Sb_2O_4 undergoes further reaction to Sb in a similar manner.

The reduction process of Sb_2O_3 and TeO_2 mixed oxides is different from what could be expected from the single oxide processes. Evaluation of samples' phase composition reveals, that redox reaction $2Sb_2O_3+TeO_2 \rightarrow 2Sb_2O_4+Te$ takes place. A similar phenomenon was observed in the $Bi_2O_3+Sb_2O_3$ as well as in the three oxide mixture system. This process is direct, however, a parallel mechanism, in which hydrogen reduces TeO_2 and emerging water oxidizes Sb_2O_3 to Sb_2O_4 cannot be excluded. At 700 K, the self-heating effect related to elemental tellurium was observed. The antimony oxide Sb_2O_3 undergoes reduction at lower temperatures when it is a component of the mixture. During the reduction of the $Bi_2O_3+Sb_2O_3$ mixture, in addition to the formation of the Sb_2O_4 by-product, the two oxides influence the reduction of each other by increasing the onset temperature of the reduction of Bi_2O_3 and decreasing this value for Sb_2O_3. The obtained kinetic parameters are in agreement with those of the corresponding single oxide reduction processes.

At the beginning of the three mixed oxides ($Bi_2O_3+Sb_2O_3+6TeO_2$) the obtained TGA results and calculated kinetic parameters are similar to those of the antimony and tellurium oxides mixture. This is a consequence of the fact that oxidation of Sb_2O_3 to Sb_2O_4 and reduction of the latter oxide is a limiting mechanism at the beginning of the reduction of the three oxides. Further, the increase in the reaction rate at 700 K, resulting from the self-heating (related to elemental Te) is observed only in the 2 K/min measurement. For higher heating rates, the onset temperature of the reaction acceleration shifts towards 730 K. The shift is related to a different mechanism - onset of the Sb_2O_3 reduction - related to the maximum. At the end of the process, the results of the kinetic analysis are similar to those found for the reduction of mixed bismuth and tellurium oxides. Another similarity is in the structural changes of the powder. The most growing grains are those of the $(Bi,Sb)_2Te_3$ phase. The growth of the obtained phase grains during the reduction process seems to be limited by the presence of oxide particles.

Analysis of the results shows, that a generalised description of the reduction process of the Bi, Sb and Te mixed oxides cannot be given. The presence or absence of any of the oxides significantly changes mechanisms of the overall reaction and elemental processes and their by-products. In the non-isothermal conditions applied, the heating rate also plays an important role.

Author statement

Bartosz Trawiński: Conceptualization, Methodology, Software, Validation, Formal analysis, Investigation, Data Curation, Writing - Original Draft, Writing - Review & Editing, Visualization

Bogusław Kusz: Conceptualization, Methodology, Resources, Writing - Review & Editing, Supervision, Project administration, Funding acquisition

Declaration of Competing Interest

The authors declare that they have no known competing financial interests or personal relationships that could have appeared to influence the work reported in this paper.

Acknowledgements

The authors would like to acknowledge Dr Jakub Karczewski for SEM imaging. This work was supported by National Science Centre Poland [grant number 2016/21/B/ST8/03193].

Appendix A. Supplementary data

Supplementary material related to this article can be found, in the online version, at doi:https://doi.org/10.1016/j.tca.2021.178966.

References

[1] J.A. Rodriguez, J.C. Hanson, A.I. Frenkel, J.Y. Kim, M. Pérez, Experimental and theoretical studies on the reaction of H2 with NiO: role of O vacancies and mechanism for oxide reduction, J. Am. Chem. Soc. 124 (2002) 346–354, https://doi.org/10.1021/ja0121080.

[2] P. Pourghahramani, E. Forssberg, Reduction kinetics of mechanically activated hematite concentrate with hydrogen gas using nonisothermal methods, Thermochim. Acta 454 (2007) 69–77, https://doi.org/10.1016/j.tca.2006.12.023.

[3] S. Vyazovkin, A time to search: finding the meaning of variable activation energy, Phys. Chem. Chem. Phys. 18 (2016) 18643–18656, https://doi.org/10.1039/C6CP02491B.

[4] B. Trawiński, B. Bochentyn, B. Kusz, A study of a reduction of a micro- and nanometric bismuth oxide in hydrogen atmosphere, Thermochim. Acta 669 (2018) 99–108, https://doi.org/10.1016/J.TCA.2018.09.010.

[5] B. Trawiński, B. Bochentyn, M. Łapiński, B. Kusz, A study of the kinetics of bismuth telluride synthesis by an oxide reduction method, Thermochim. Acta 683 (2020), https://doi.org/10.1016/J.TCA.2019.178437, 178437.

[6] M.M. Hossain, S. Ahmed, Cu-based mixed metal oxide catalysts for WGSR: reduction kinetics and catalytic activity, Can. J. Chem. Eng. 91 (2013) 1450–1458, https://doi.org/10.1002/cjce.21758.

[7] M.A.Nasr A. Omar, M.H. Khedr, A.A. El Geassy, Effect of nickel oxide doping on the kinetics and mechanism of lron oxide reduction, ISIJ Int. 35 (1995) 43–1049, https://doi.org/10.2355/isijinternational.35.1043.

[8] Y. Jin, Y. Liu, Y. Wang, J. Ye, Study on phase evolution during reaction synthesis of ultrafine (Ti, W, Mo, V)(CN)-Ni composite powders, Mater. Chem. Phys. 118 (2009) 191–196, https://doi.org/10.1016/j.matchemphys.2009.07.021.

[9] M. Ghoussoub, P.N. Duchesne, M. Xia, A. Jelle, S. He, N. Soheilnia, G.A. Ozin, Kinetics and mechanism of turanite reduction by hydrogen, J. Phys. Chem. C. 124 (2020) 18356–18365, https://doi.org/10.1021/acs.jpcc.0c05428.

[10] Y. lei Sui, Y. feng Guo, T. Jiang, G. zhou Qiu, Reduction kinetics of oxidized vanadium titano-magnetite pellets using carbon monoxide and hydrogen, J. Alloys. Compd. 706 (2017) 546–553, https://doi.org/10.1016/j.jallcom.2017.02.264.

[11] V.B. Chernogorenko, K.A. Lynchak, Z.A. Klimak, R.A. Morozova, Kinetics of antimony trioxide reduction by hydrogen. Effect of atomic hydrogen, Sov. Powder Metall. Met. Ceram. 17 (1978) 419–421, https://doi.org/10.1007/BF00795791.

[12] A. Khawam, D.R. Flanagan, Role of isoconversional methods in varying activation energies of solid-state kinetics: II. Nonisothermal kinetic studies, Thermochim. Acta 436 (2005) 101–112, https://doi.org/10.1016/j.tca.2005.05.015.

[13] S. Vyazovkin, A.K. Burnham, J.M. Criado, L.A. Pérez-Maqueda, C. Popescu, N. Sbirrazzuoli, ICTAC Kinetics Committee recommendations for performing kinetic computations on thermal analysis data, Thermochim. Acta 520 (2011) 1–19, https://doi.org/10.1016/j.tca.2011.03.034.

[14] J.D. Sewry, M.E. Brown, "Model-free" kinetic analysis? Thermochim. Acta 390 (2002) 217–225, https://doi.org/10.1016/S0040-6031(02)00083-7.

[15] R. Serra, J. Sempere, R. Nomen, A new method for the kinetic study of thermoanalytical data: the non-parametric kinetics method, Thermochim. Acta 316 (1998) 37–45, https://doi.org/10.1016/S0040-6031(98)00295-0.

[16] J. Šesták, Šesták-Berggren equation: now questioned but formerly celebrated-what is right, J. Therm. Anal. Calorim. 217 (2017) 1117–1123, https://doi.org/10.1007/s10973-015-4998-x.

[17] L.A. Pérez-Maqueda, J.M. Criado, P.E. Sánchez-Jiménez, Combined kinetic analysis of solid-state reactions: a powerful tool for the simultaneous determination of kinetic parameters and the kinetic model without previous assumptions on the reaction mechanism, J. Phys. Chem. A 110 (2006) 12456–12462, https://doi.org/10.1021/jp064792g.

[18] B. Janković, B. Adnad, S. Mentus, The kinetic analysis of non-isothermal nickel oxide reduction in hydrogen atmosphere using the invariant kinetic parameters method, Thermochim. Acta 456 (2007) 48–55, https://doi.org/10.1016/j.tca.2007.01.033.

[19] M.E. Brown, Stocktaking in the kinetics cupboard, J. Therm. Anal. Calorim. 82 (2005) 665–669, https://doi.org/10.1007/s10973-005-0947-4.

[20] T. Karlsson, C. Forsgren, B.M. Steenari, Recovery of antimony: a laboratory study on the thermal decomposition and carbothermal reduction of Sb(III), Bi(III), Zn(II) oxides, and antimony compounds from metal oxide varistors, J. Sustain. Metall. 4 (2018) 194–204, https://doi.org/10.1007/s40831-017-0156-y.

[21] M.A.K. Ahmed, H. Fjellvåg, A. Kjekshus, Synthesis, structure and thermal stability of tellurium oxides and oxide sulfate formed from reactions in refluxing sulfuric acidf, J. Chem. Soc. Dalt. Trans. (2000) 4542–4549, https://doi.org/10.1039/b005688j.

[22] R.G. Orman, D. Holland, Thermal phase transitions in antimony (III) oxides, J. Solid State Chem. 180 (2007) 2587–2596, https://doi.org/10.1016/j.jssc.2007.07.004.

[23] Y. Feutelais, G. Morgant, J.R. Didry, J. Schnitter, Thermodynamic evaluation of the system bismuth-antimony, Calphad. 16 (1992) 111–119, https://doi.org/10.1016/0364-5916(92)90001-E.

[24] I.I. Ivanov, V.M. Shelemetyev, R.S. Askhadullin, A study on the kinetics of bismuth oxide reduction by hydrogen as applied to the technology of removing hydrogen from circulation circuits with heavy liquid metal coolants, Nucl. Energy Technol. 5 (2019) 331–336, https://doi.org/10.3897/nucet.5.48425.

[25] S. Vyazovkin, A.K. Burnham, L. Favergeon, N. Koga, E. Moukhina, L.A. Pérez-Maqueda, N. Sbirrazzuoli, ICTAC Kinetics Committee recommendations for analysis of multi-step kinetics, Thermochim. Acta 689 (2020), https://doi.org/10.1016/j.tca.2020.178597, 178597.

[26] H. Okamoto, Bi-Sb (Bismuth-Antimony), J. Phase Equilibria Diffus. 33 (2012) 493–494, https://doi.org/10.1007/s11669-012-0092-2.

[27] W.R. Morcom, W.L. Worrell, H.G. Sell, H.I. Kaplan, The Preparation and Characterization of Beta-Tungsten, a Metastable Tungsten Phase, n.d.

[28] D.T. Hawkins, W.L. Worrell, Hydrogen Reduction of MoO3 at Temperatures Between 300 ~ and 450~, 1970.

[29] J.I. Goldstein, D.E. Newbury, J.R. Michael, N.W.M. Ritchie, J.H.J. Scott, D.C. Joy, J.I. Goldstein, D.E. Newbury, J.R. Michael, N.W.M. Ritchie, J.H.J. Scott, D.C. Joy, Backscattered electrons. Scanning Electron Microsc. X-Ray Microanal, Springer, New York, 2018, pp. 15–28, https://doi.org/10.1007/978-1-4939-6676-9_2.

Supplementary Material

for

Kinetic analysis of the reduction of a ternary system of Bi, Sb and Te oxides by hydrogen for $BiSbTe_3$ synthesis

Bartosz Trawiński, Bogusław Kusz

1. Oxide powders

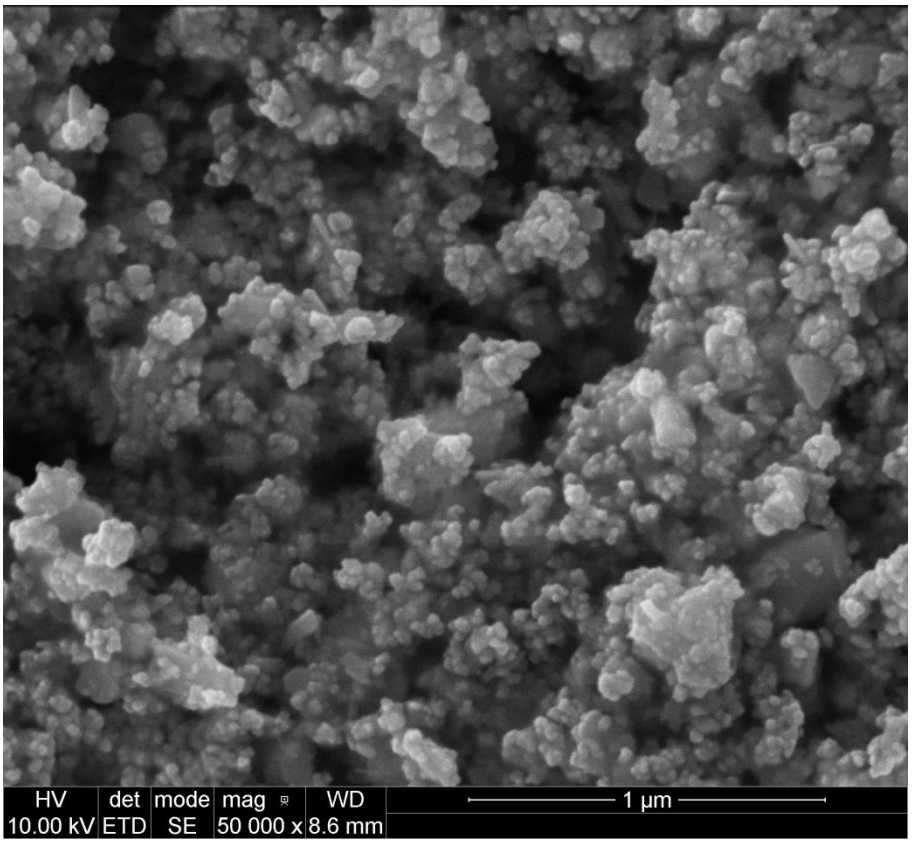

Fig. S1.1. Sb_2O_3 milled powder used in the study.

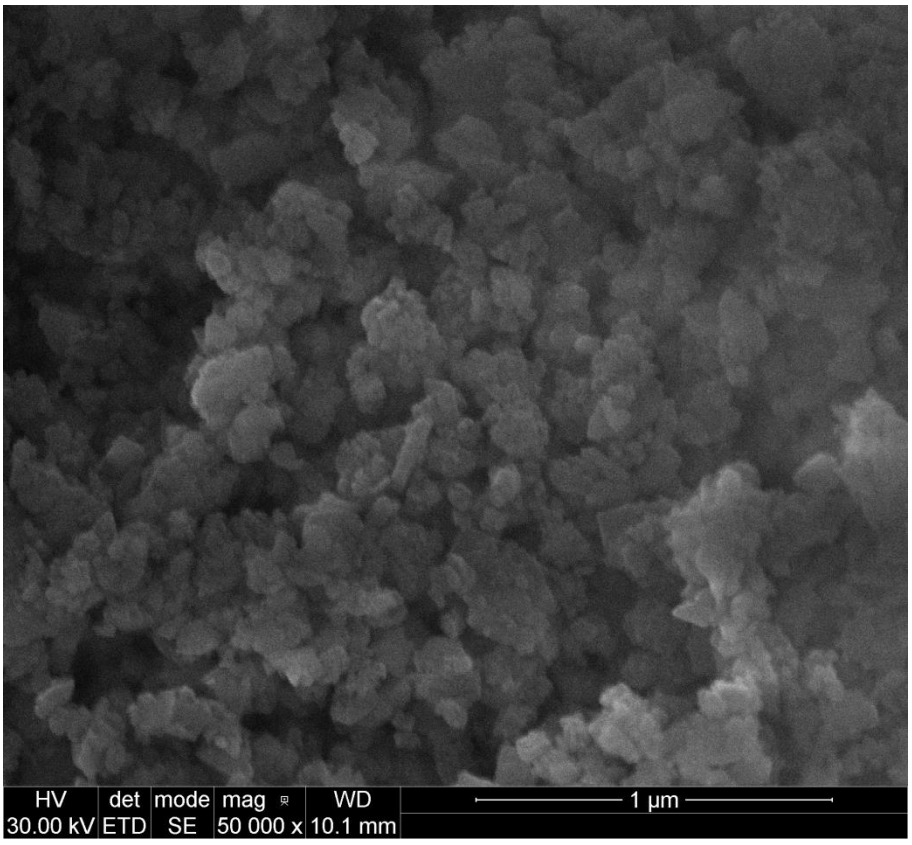

Fig. S1.2. Sb_2O_4 milled powder used in the study.

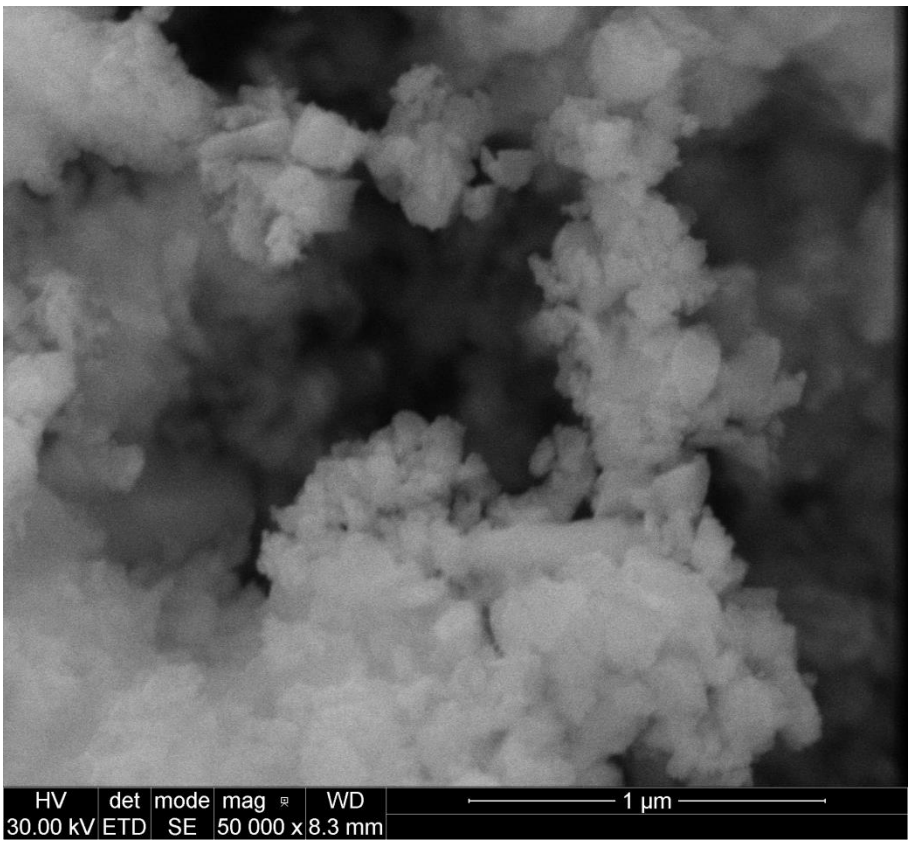

Fig. S1.3. Bi_2O_3+Sb_2O_3 milled powder used in the study.

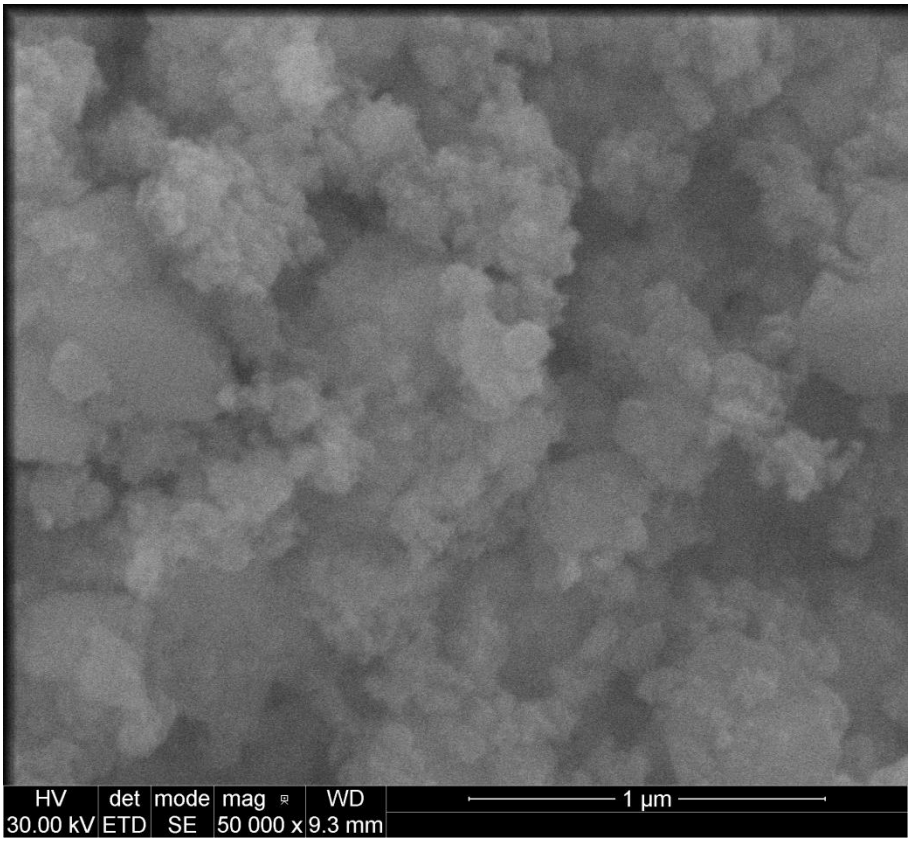

Fig. S1.4. Sb_2O_3+3TeO_2 milled powder used in the study.

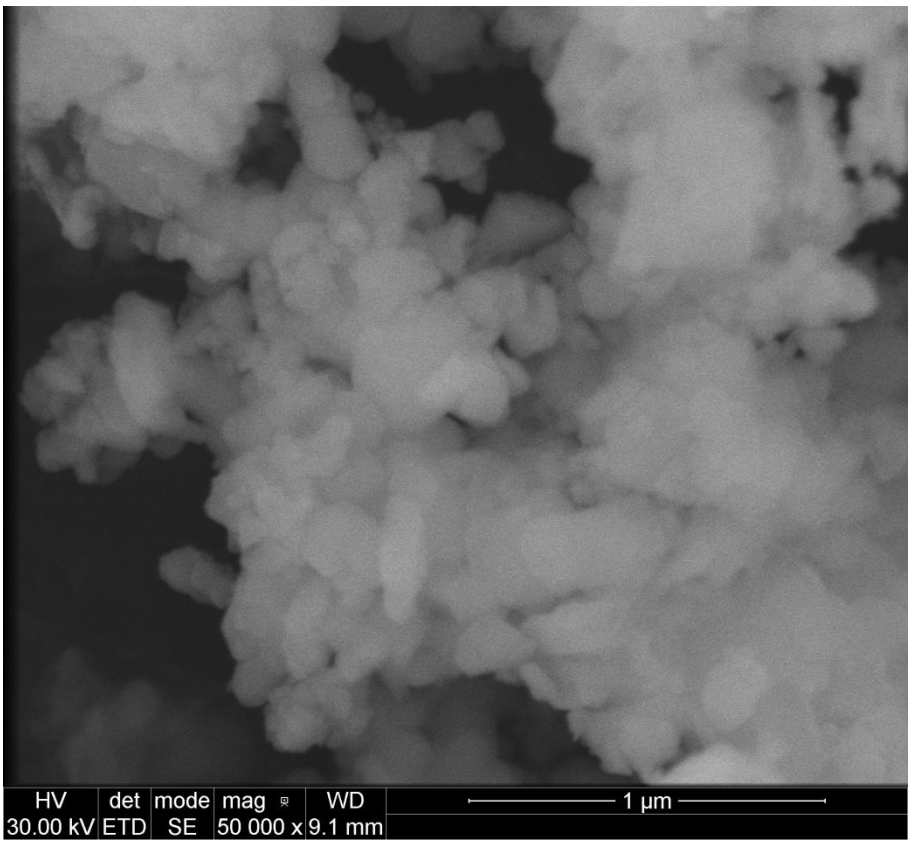

Fig. S1.5. Bi_2O_3+Sb_2O_3+6TeO_2 milled powder used in the study.

2. Sb_2O_3 reduction

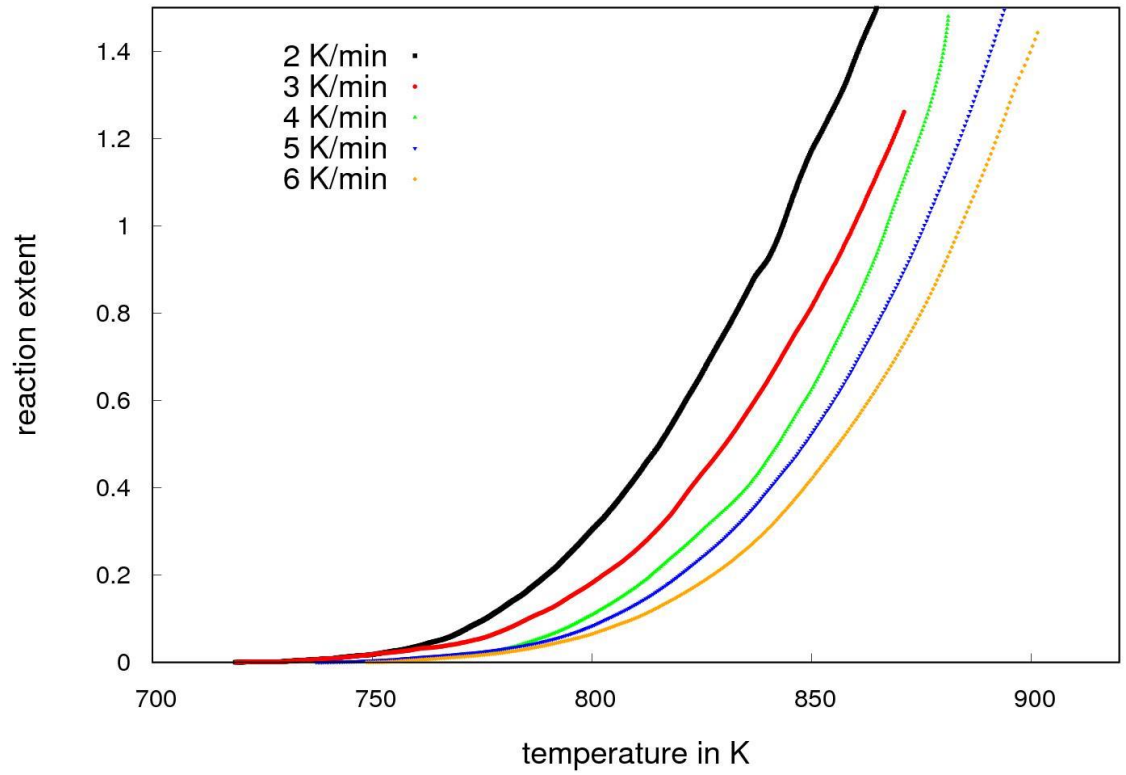

Fig. S2.1. Dependence of the reaction extent on the temperature during the reduction of Sb_2O_3.

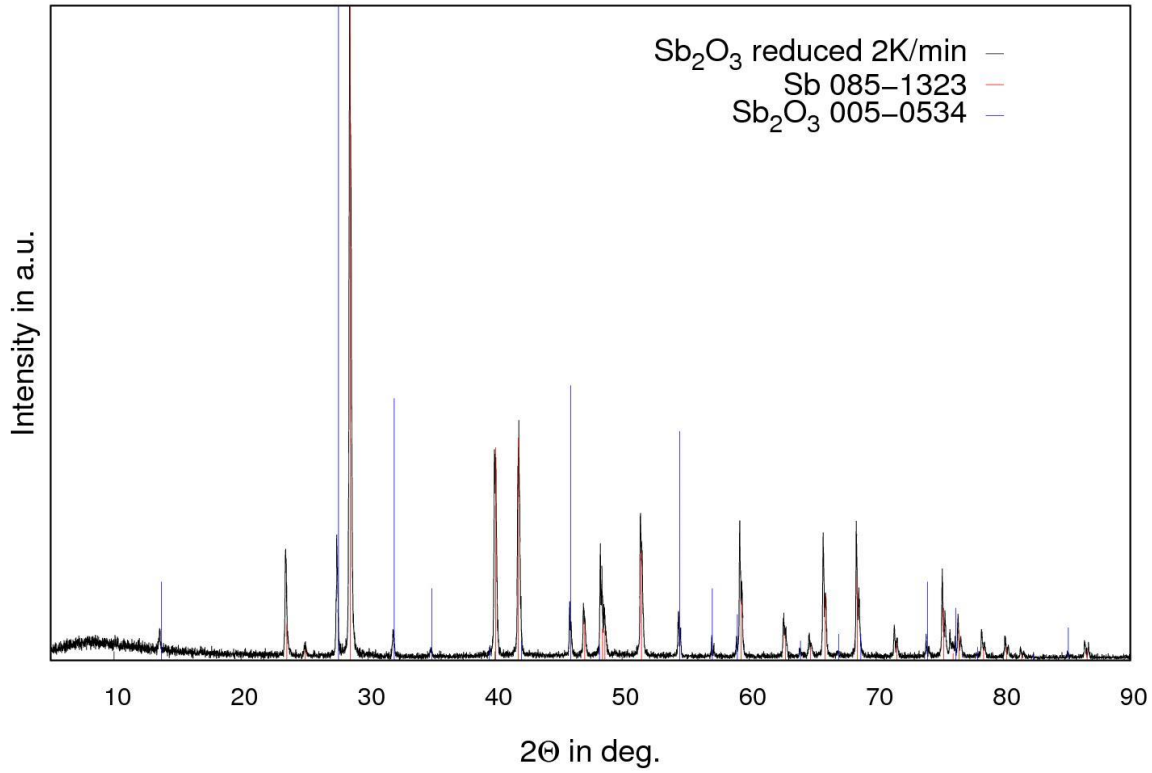

Fig. S2.2. The diffraction pattern of the Sb_2O_3 reduced up to 840 K with a 2 K/min heating rate with reference patterns.

3. Sb_2O_4 reduction

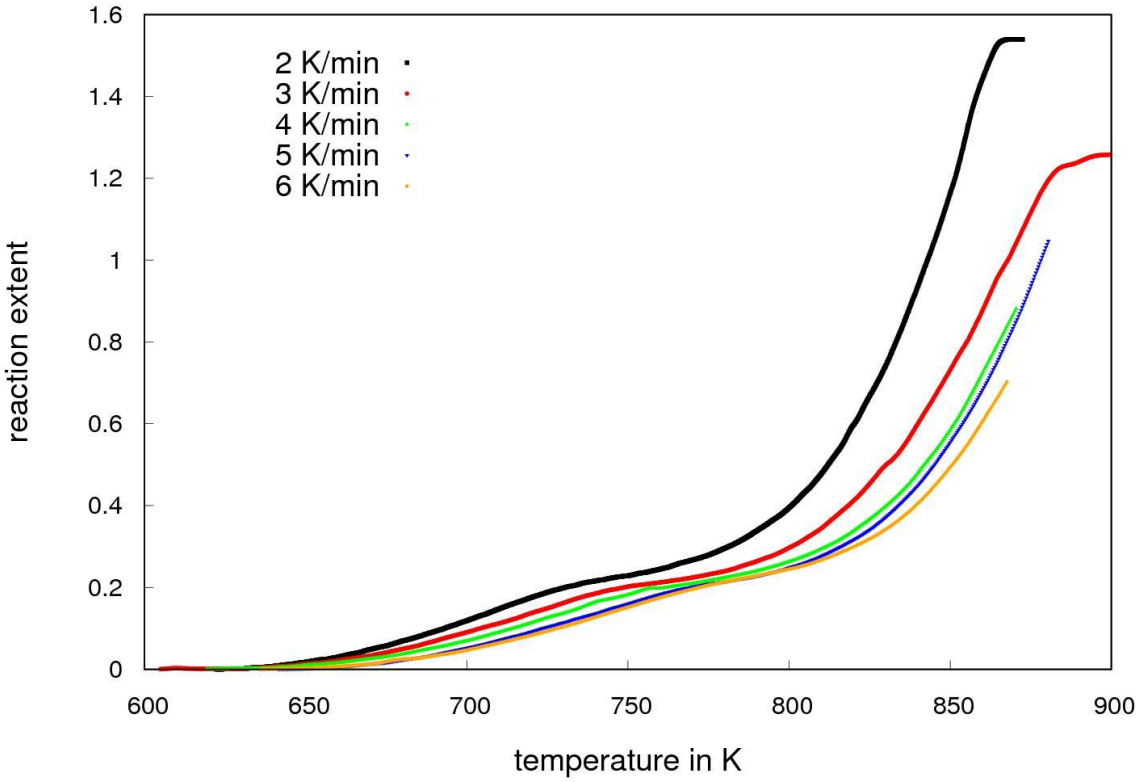

Fig. S3.1. Dependence of the reaction extent on the temperature during the reduction of Sb_2O_4.

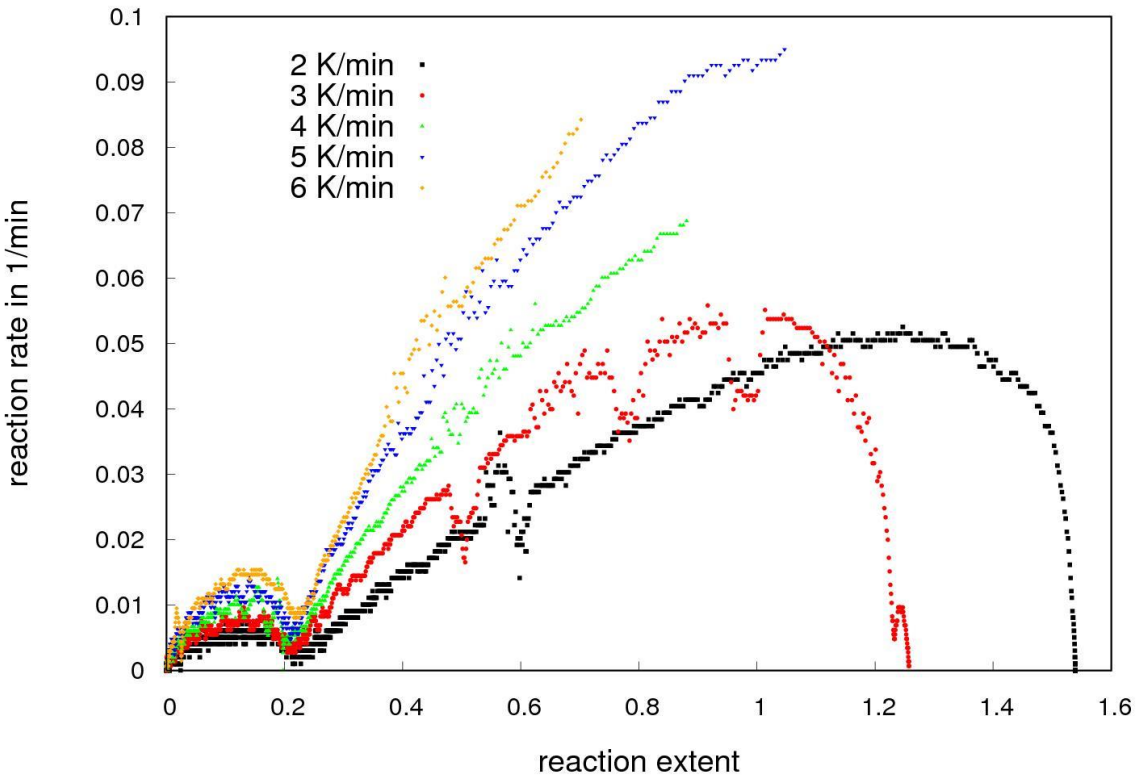

Fig. S3.2. Dependence of the reaction rate on the reaction extent during the reduction of Sb_2O_4.

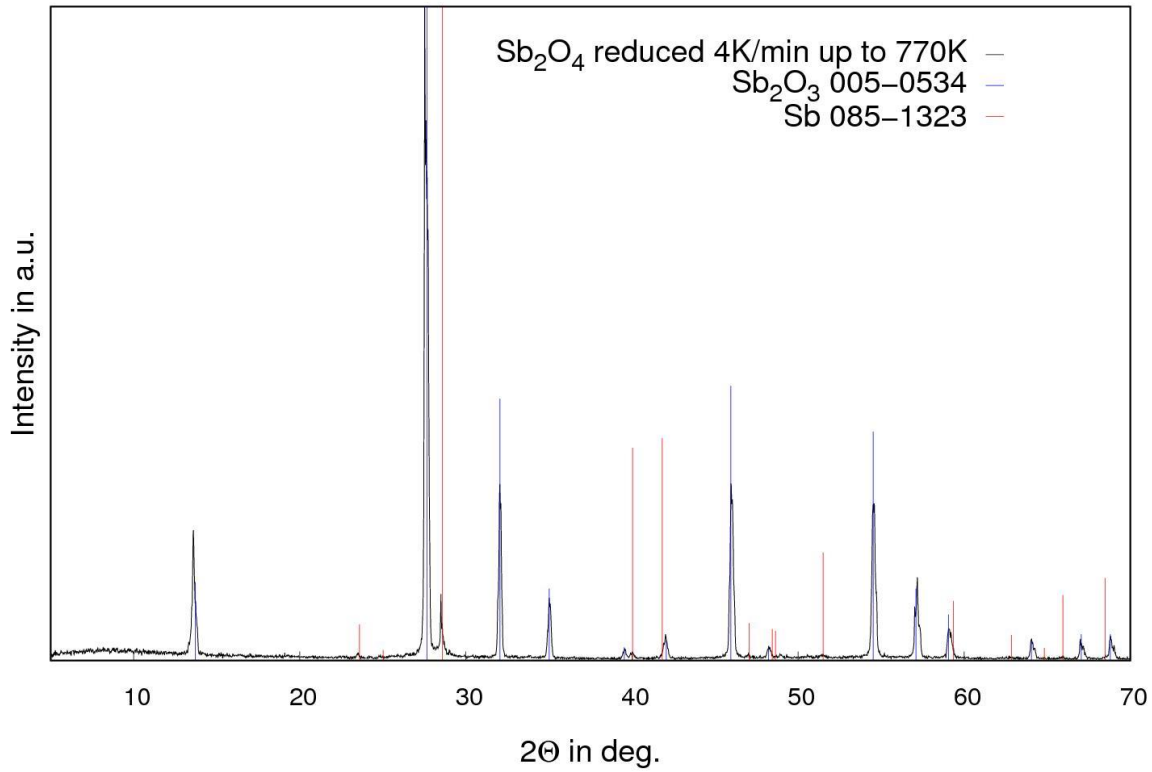

Fig. S3.3. The diffraction pattern of the Sb_2O_4 reduced up to 770 K with a 4 K/min heating rate with reference patterns.

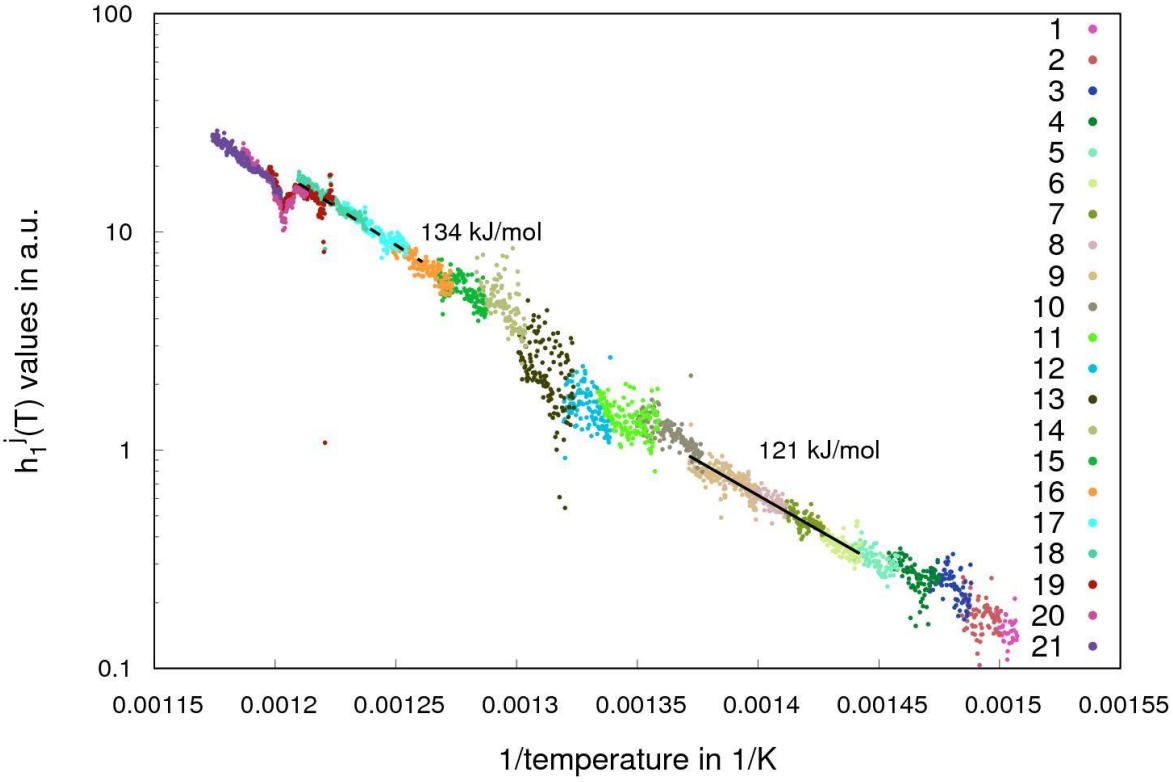

Fig. S3.4. Thermal function $h(T)$ calculated with the NPK analysis of the reduction of Sb_2O_4. Values in the key stand for j indices of vectors $\mathbf{v_1}^j$. The dashed line and the corresponding E value is for orientation only.

4. Sb_2O_3+3TeO_2 reduction

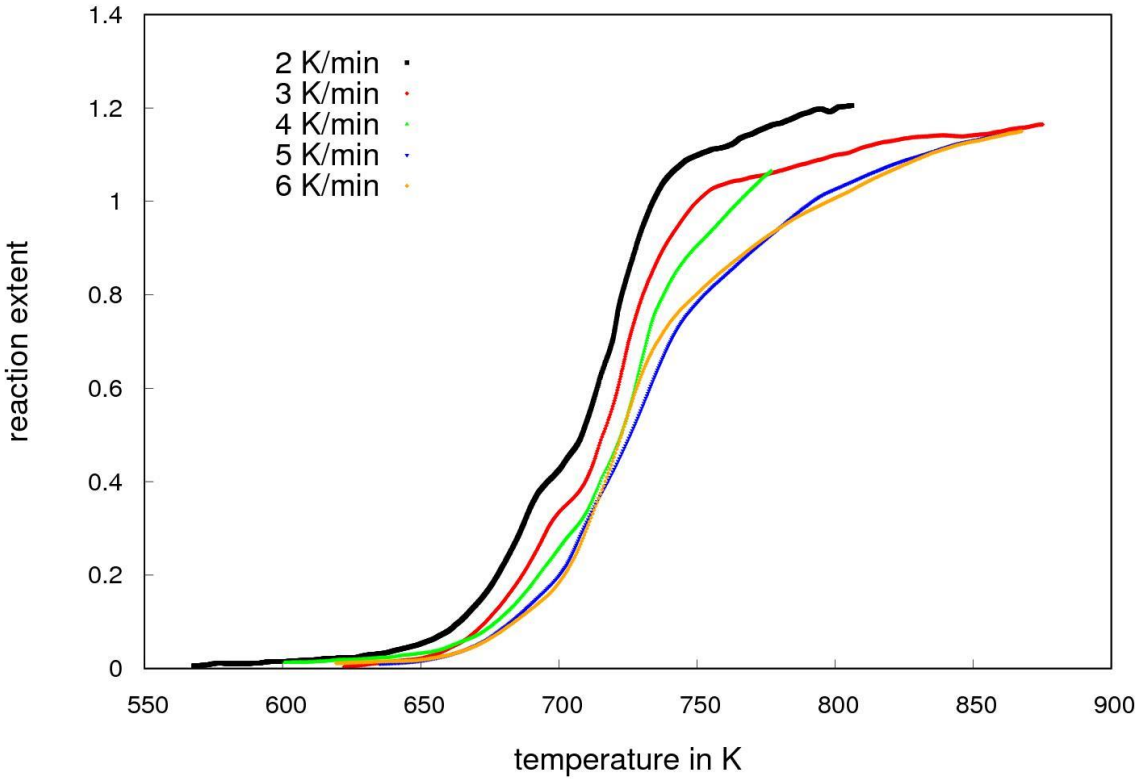

Fig. S4.1. Dependence of the reaction extent on the temperature during the reduction of Sb_2O_3+3TeO_2 mixed oxides.

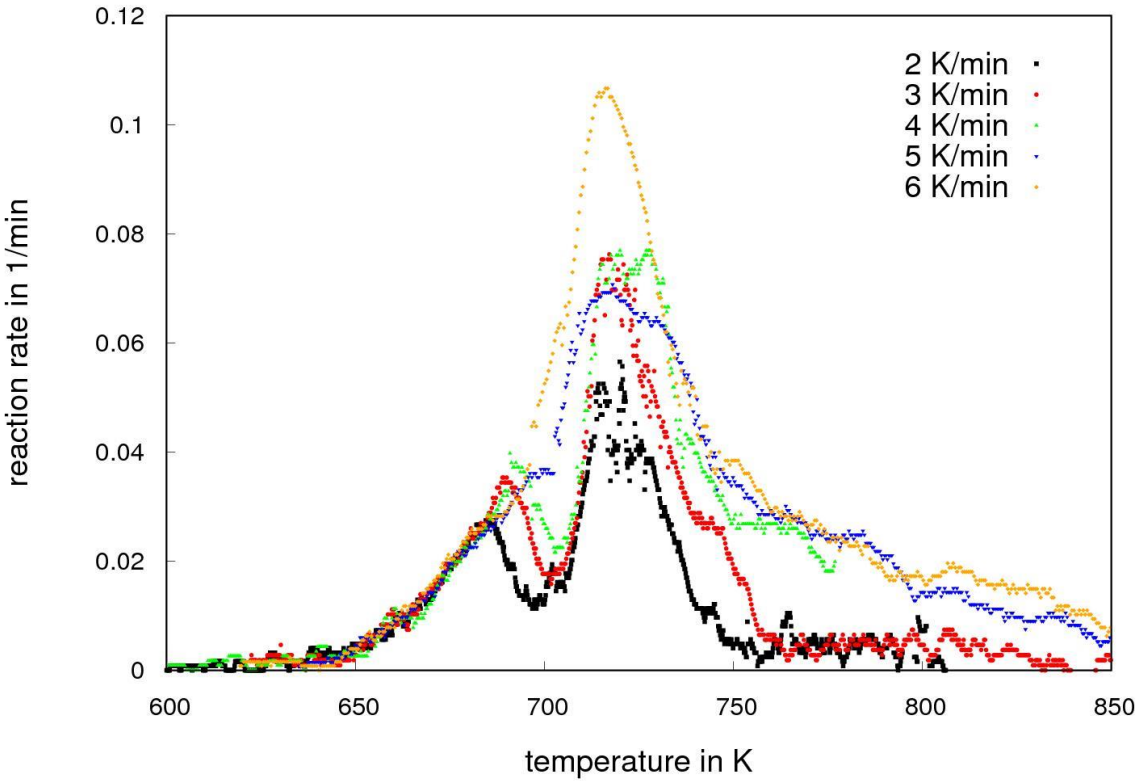

Fig. S4.2. Dependence of the reaction rate on the temperature during the reduction of Sb_2O_3+3TeO_2 mixed oxides.

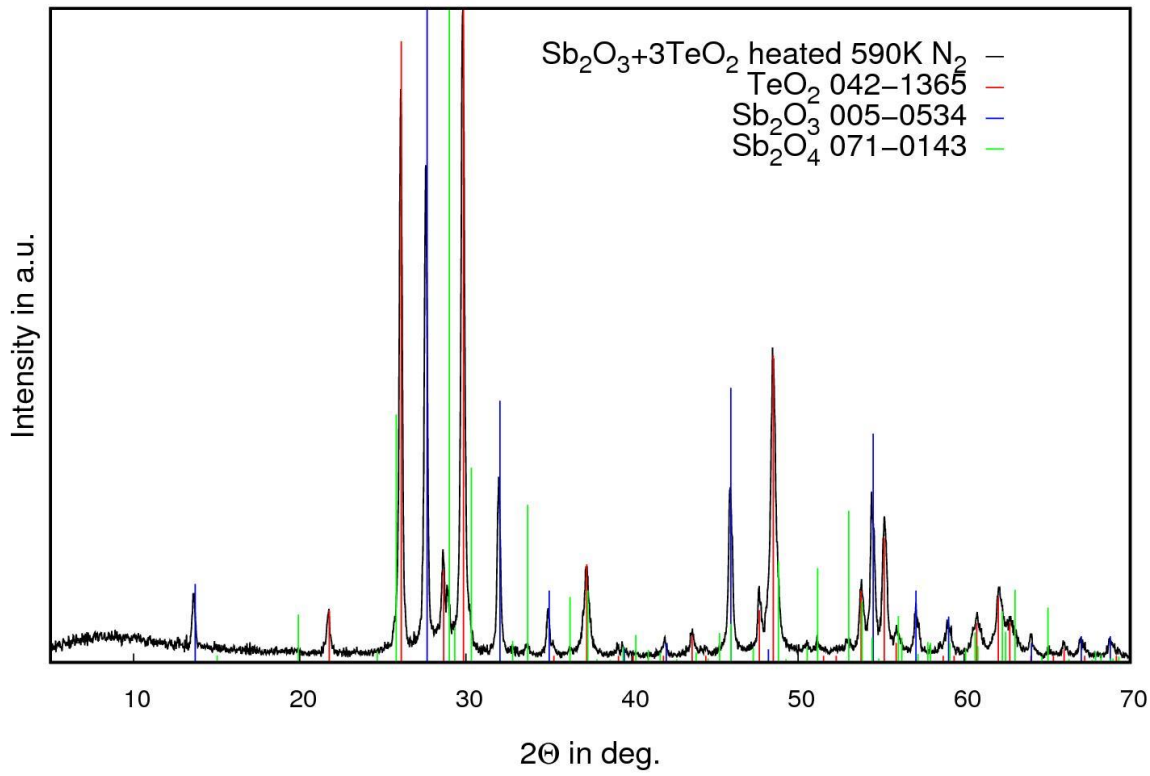

Fig. S4.3. The diffraction pattern of the Sb_2O_3+3TeO_2 powder heated the nitrogen atmosphere to 590 K with a 2 K/min heating rate with reference patterns.

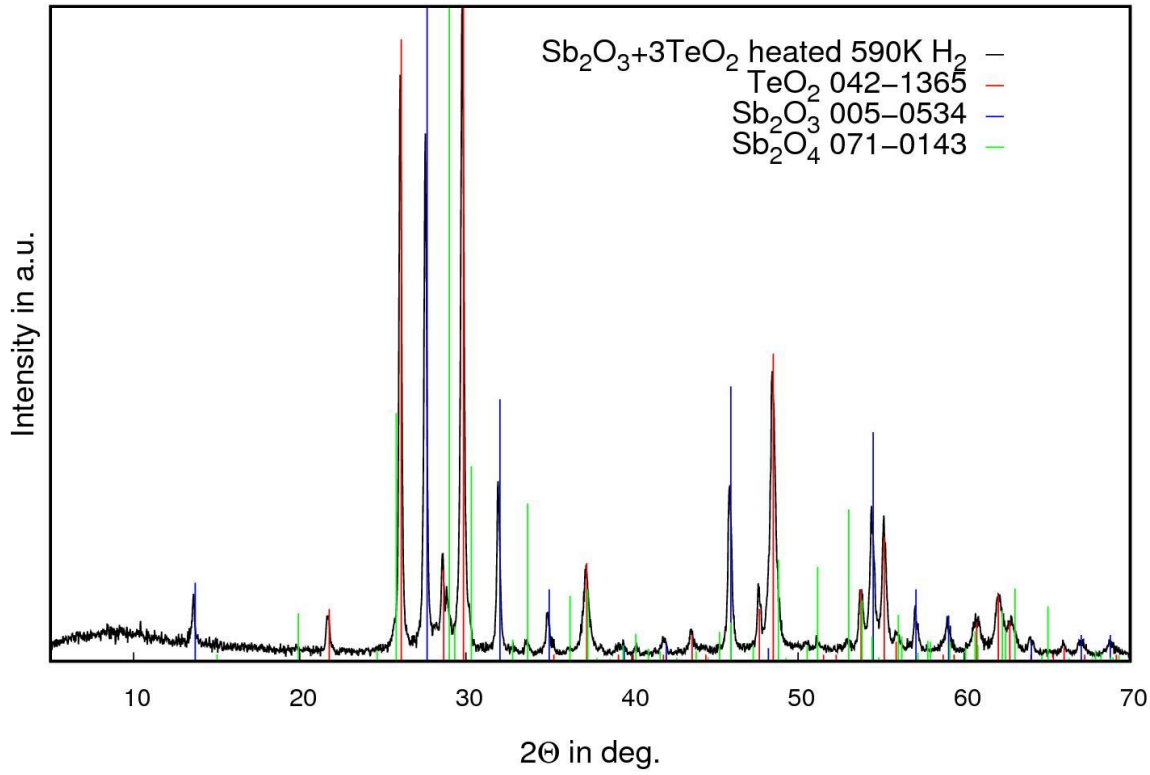

Fig. S4.4. The diffraction pattern of the Sb_2O_3+3TeO_2 powder heated the hydrogen atmosphere to 590 K with a 2 K/min heating rate with reference patterns.

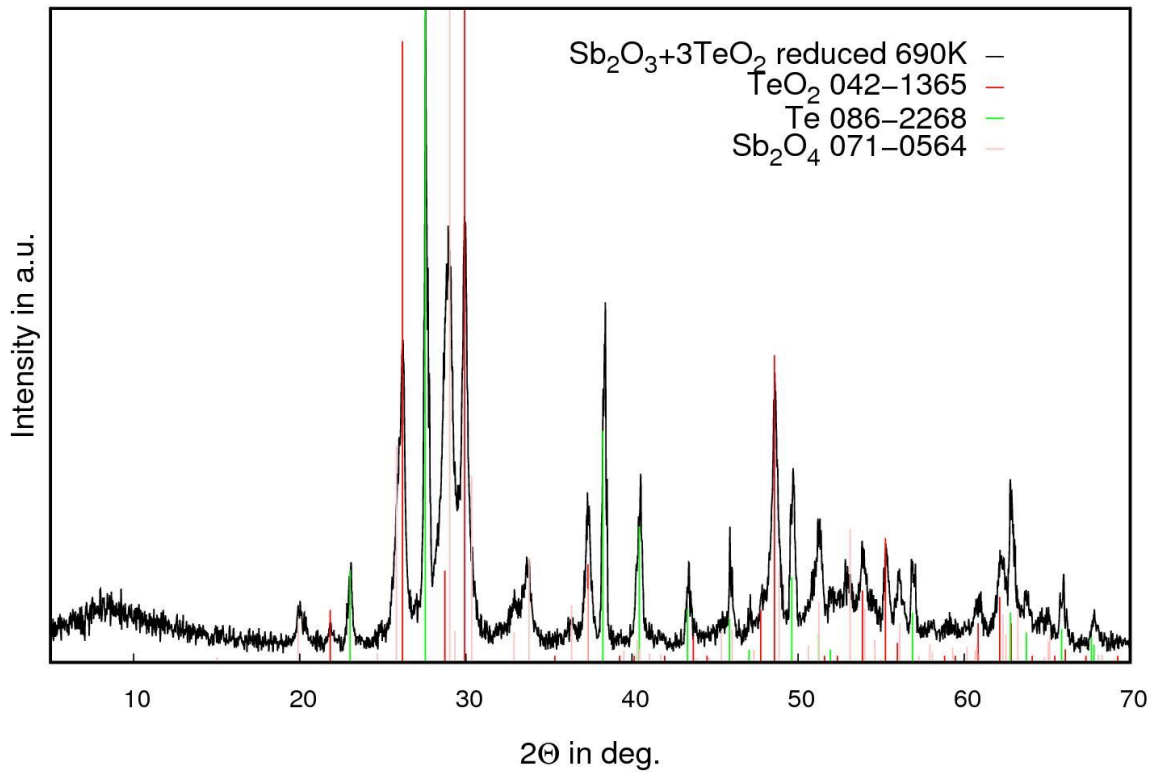

Fig. S4.5. Diffraction pattern of the Sb_2O_3+3TeO_2 powder reduced in hydrogen up to 690 K with 2 K/min heating rate with reference patterns.

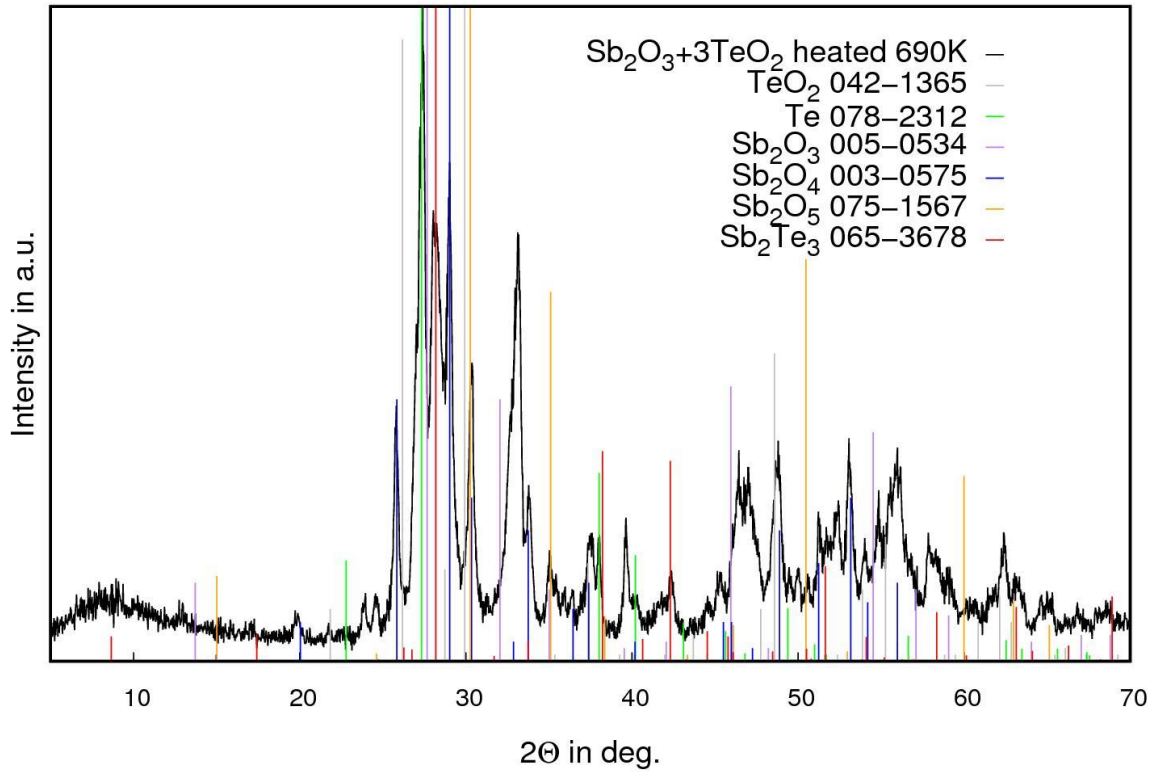

Fig. S4.6. The diffraction pattern of the Sb_2O_3+3TeO_2 powder heated the nitrogen atmosphere to 690 K with a 2 K/min heating rate with reference patterns.

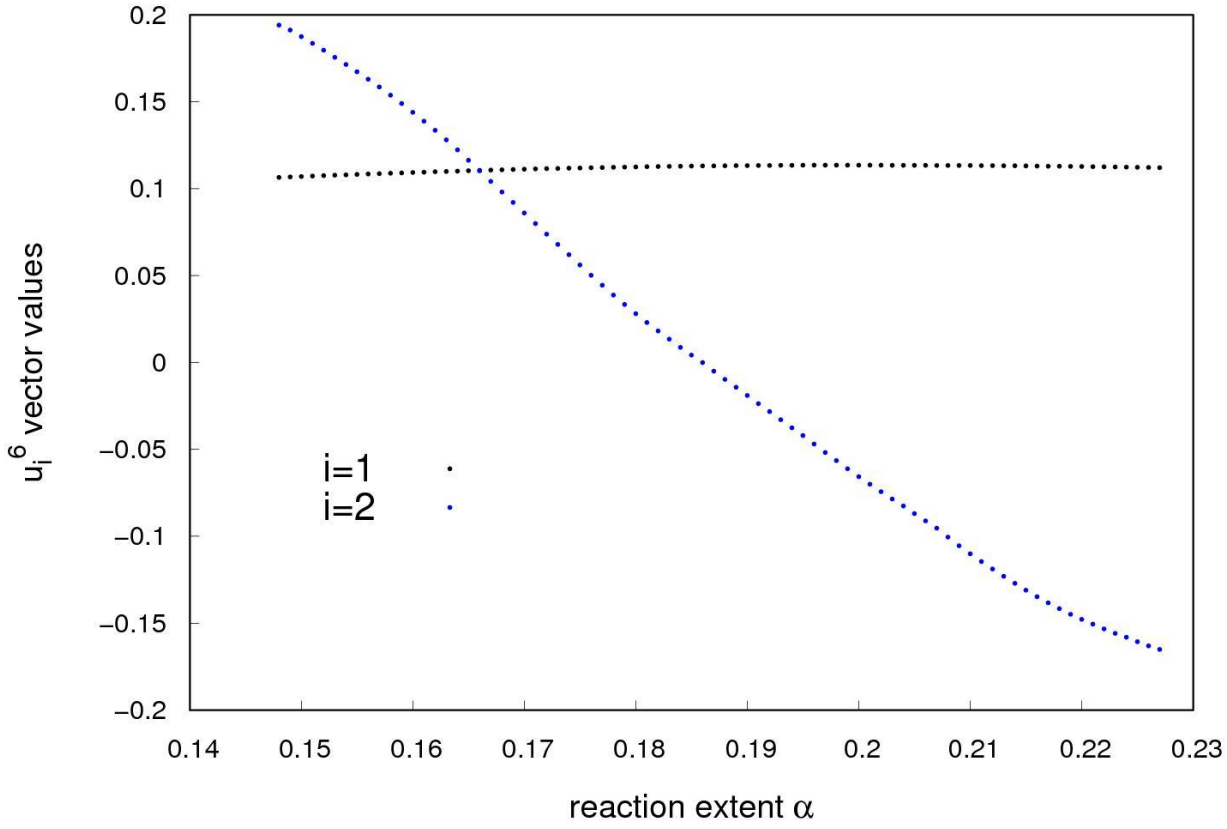

Fig. S4.7. Values of the vectors u_1^6 and u_2^6 obtained in the NPK analysis of the reduction of Sb_2O_3+3TeO_2.

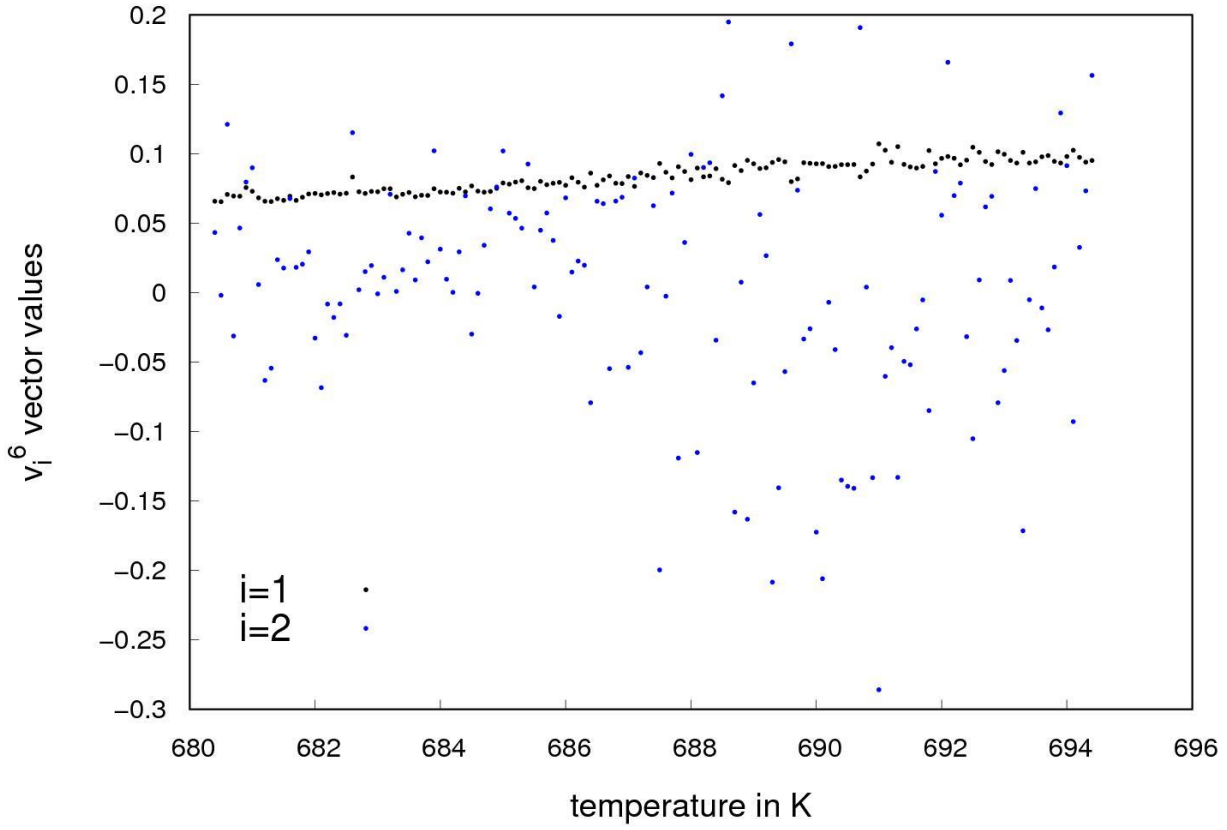

Fig. S4.8. Values of the vectors v_1^6 and v_2^6 obtained in the NPK analysis of the reduction of Sb_2O_3+3TeO_2.

5. Bi_2O_3+Sb_2O_3 reduction

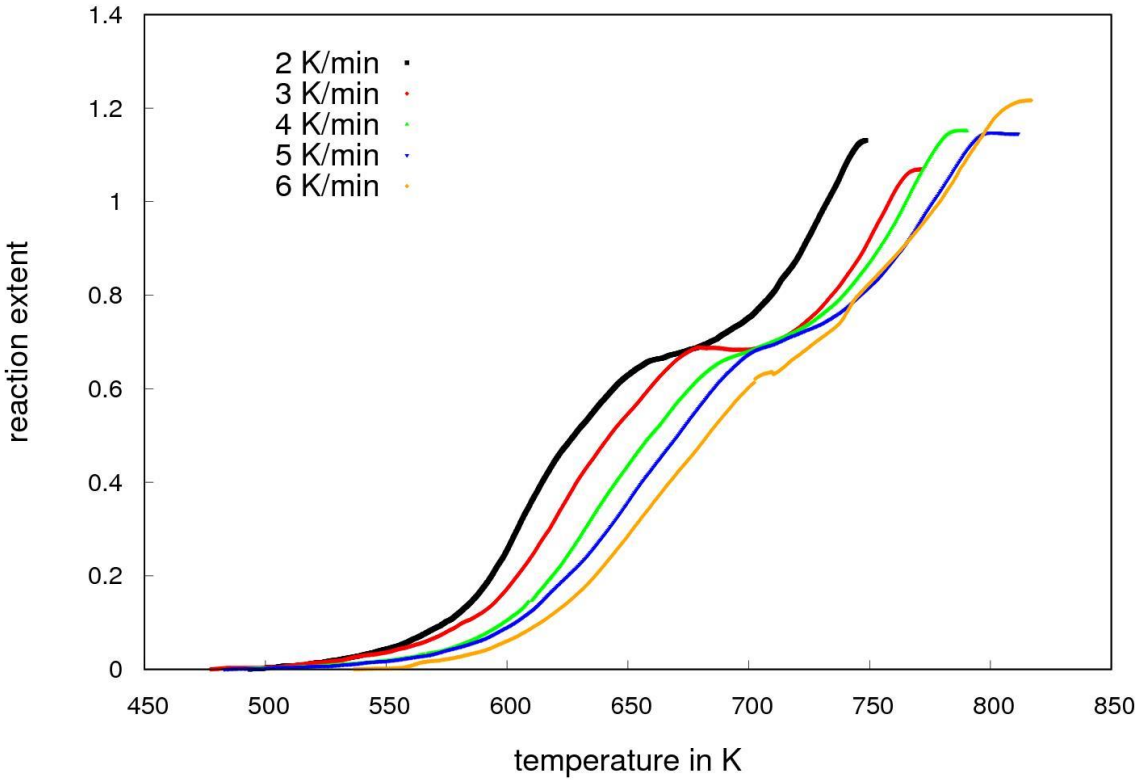

Fig. S5.1. Dependence of the reaction extent on the temperature during the reduction of Bi_2O_3+ Sb_2O_3 mixed oxides.

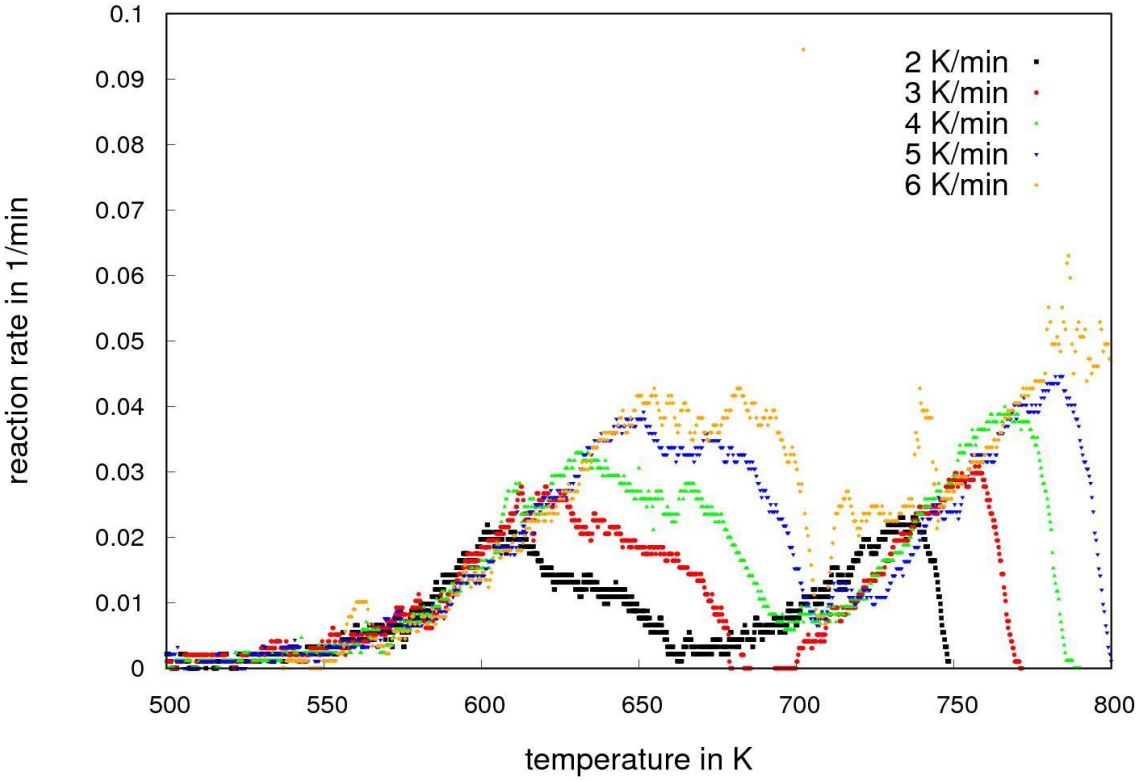

Fig. S5.2. Dependence of the reaction rate on the temperature during the reduction of Bi_2O_3+ Sb_2O_3 mixed oxides.

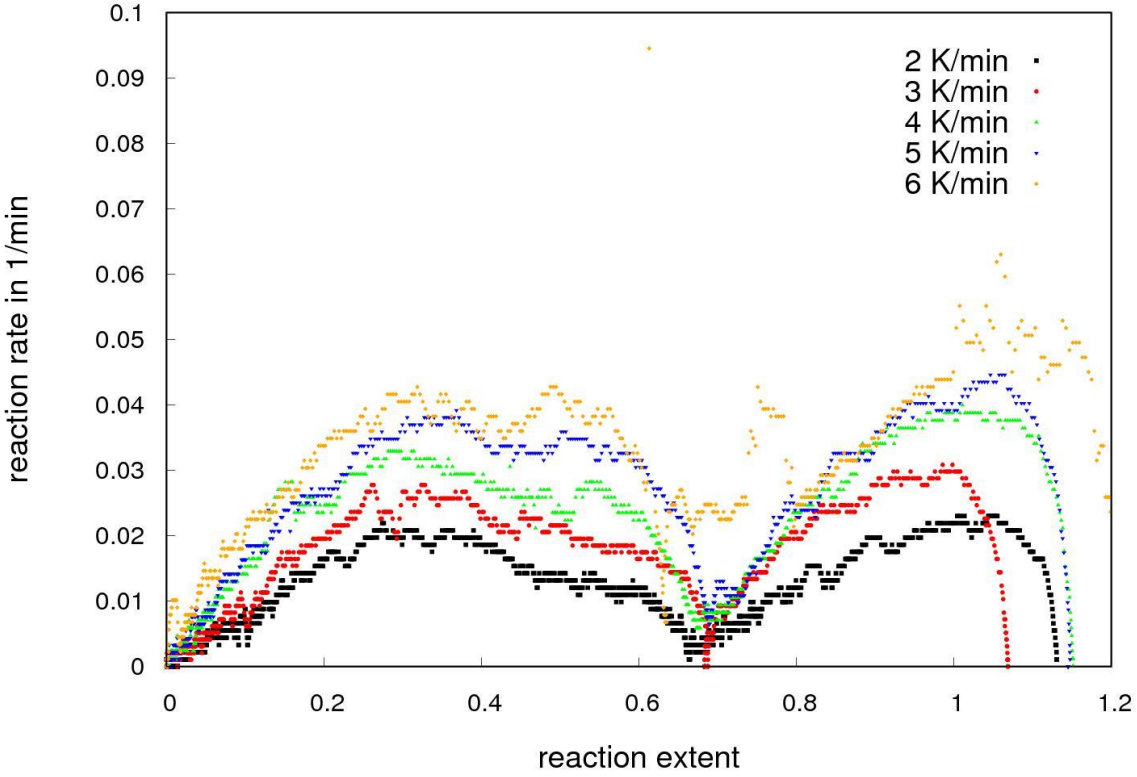

Fig. S5.3. Dependence of the reaction rate on the reaction extent during the reduction of Bi_2O_3+ Sb_2O_3 mixed oxides.

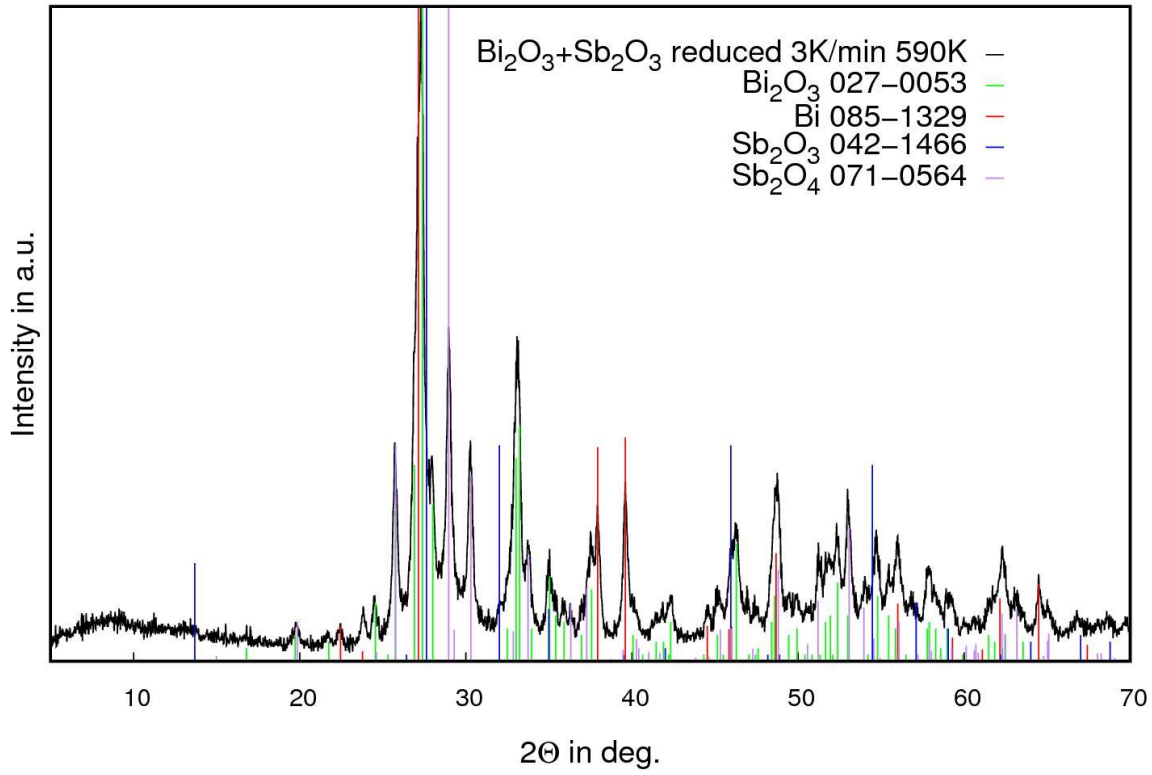

Fig. S5.4. Diffraction pattern of the Bi_2O_3+ Sb_2O_3 powder reduced in hydrogen up to 590 K with 3 K/min heating rate with reference patterns.

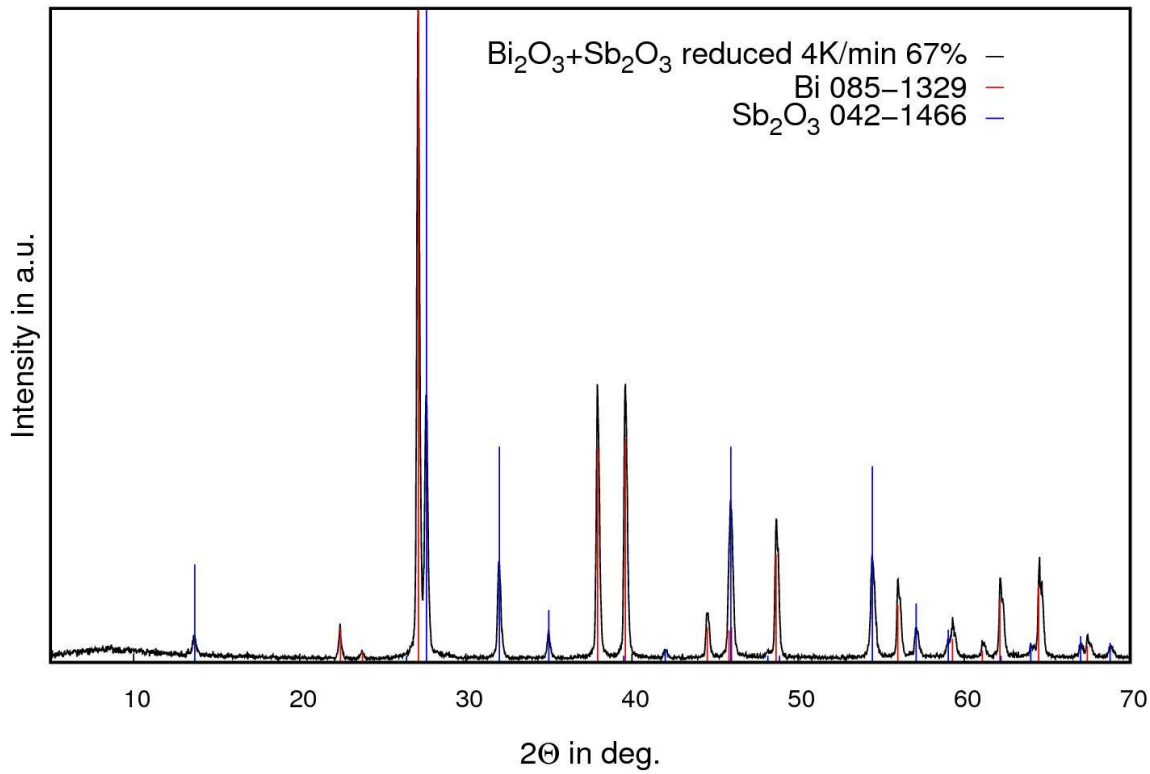

Fig. S5.5. Diffraction pattern of the Bi_2O_3+ Sb_2O_3 powder reduced in hydrogen up to 67% of the expected mass change with a 4 K/min heating rate with reference patterns.

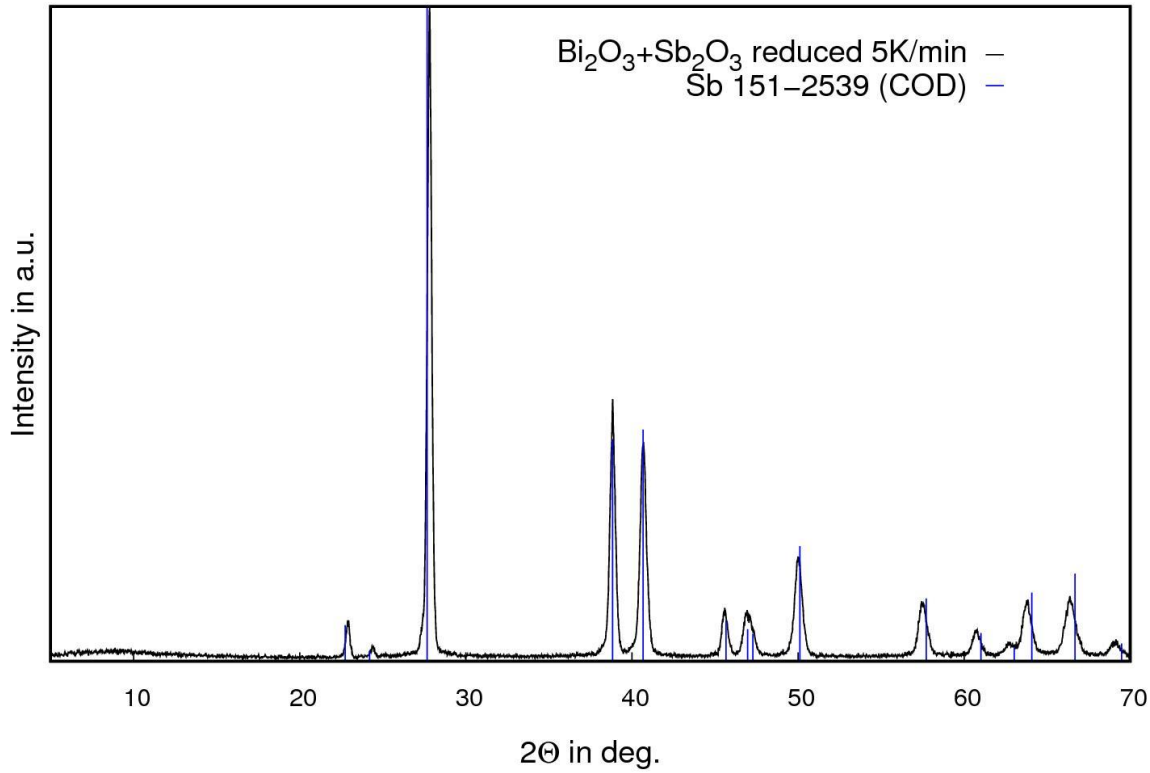

Fig. S5.6. Diffraction pattern of the Bi_2O_3+ Sb_2O_3 powder reduced in with 5 K/min heating rate with reference pattern (from Crystallography Open Database).

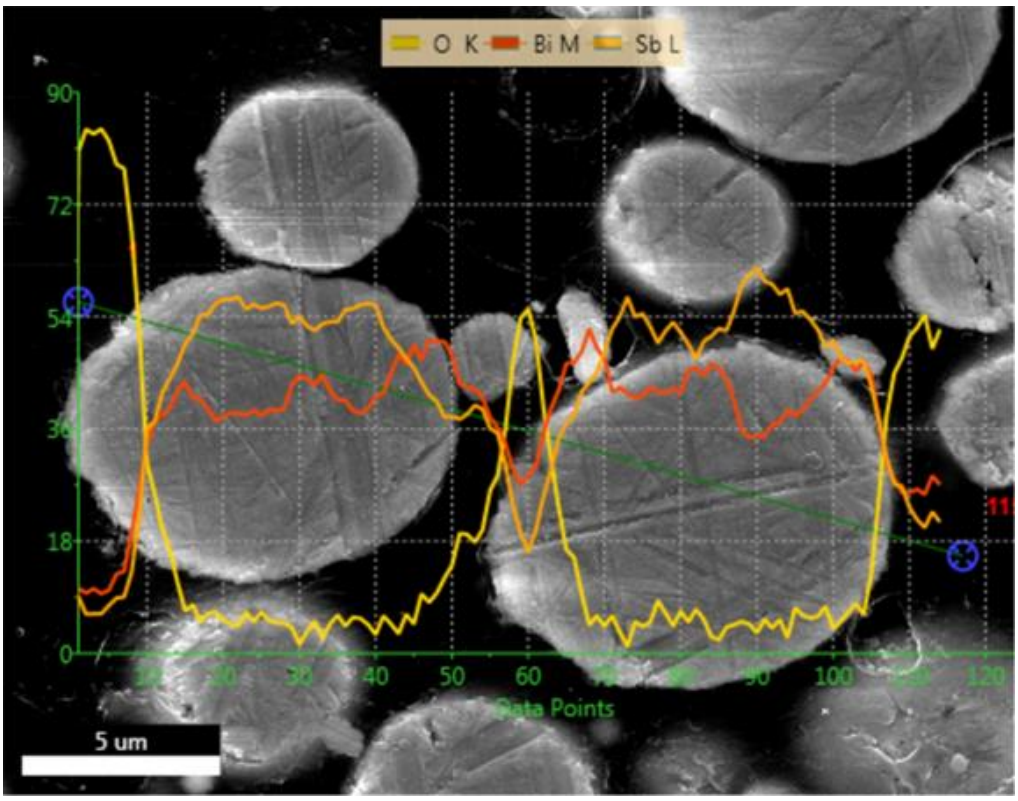

Fig. S5.7. Cross-section of the BiSb particles obtained by the reduction of oxides with 5 K/min heating rate with results of a linear EDX scan.

6. Bi_2O_3+Sb_2O_3+3TeO_2 reduction

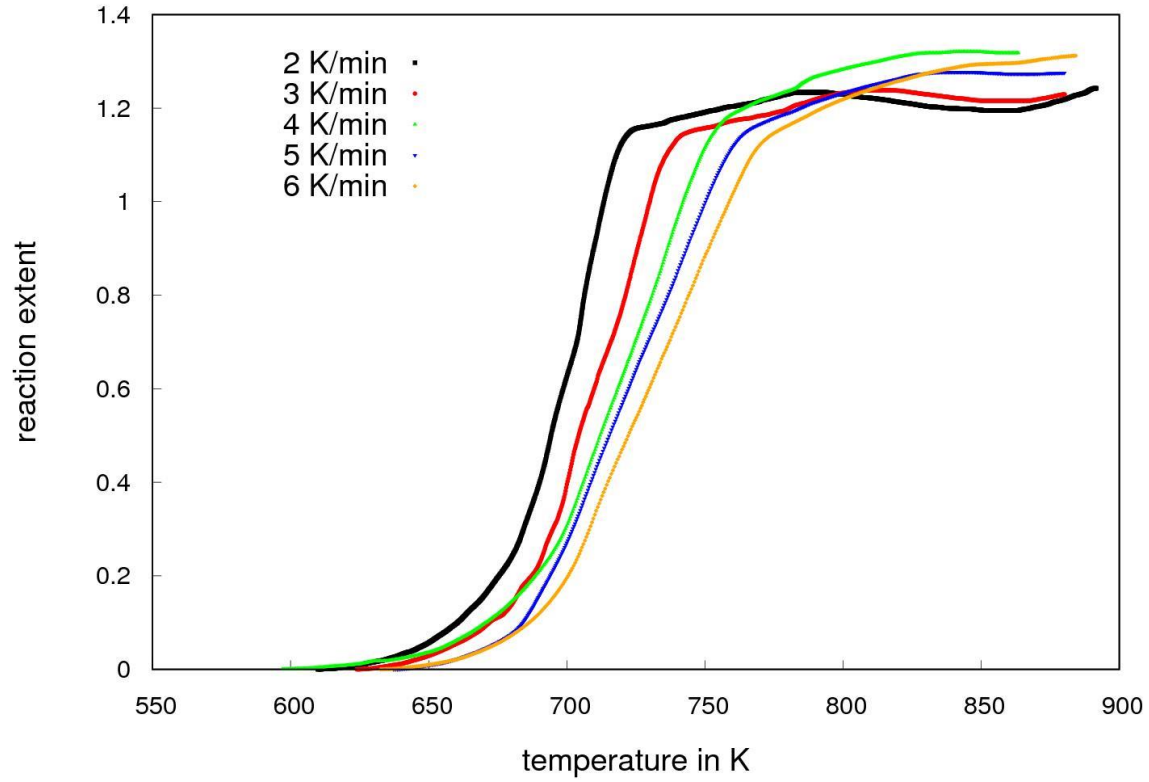

Fig. S6.1. Dependence of the reaction extent on the temperature during the reduction of Bi_2O_3+ Sb_2O_3+3TeO_2 mixed oxides.

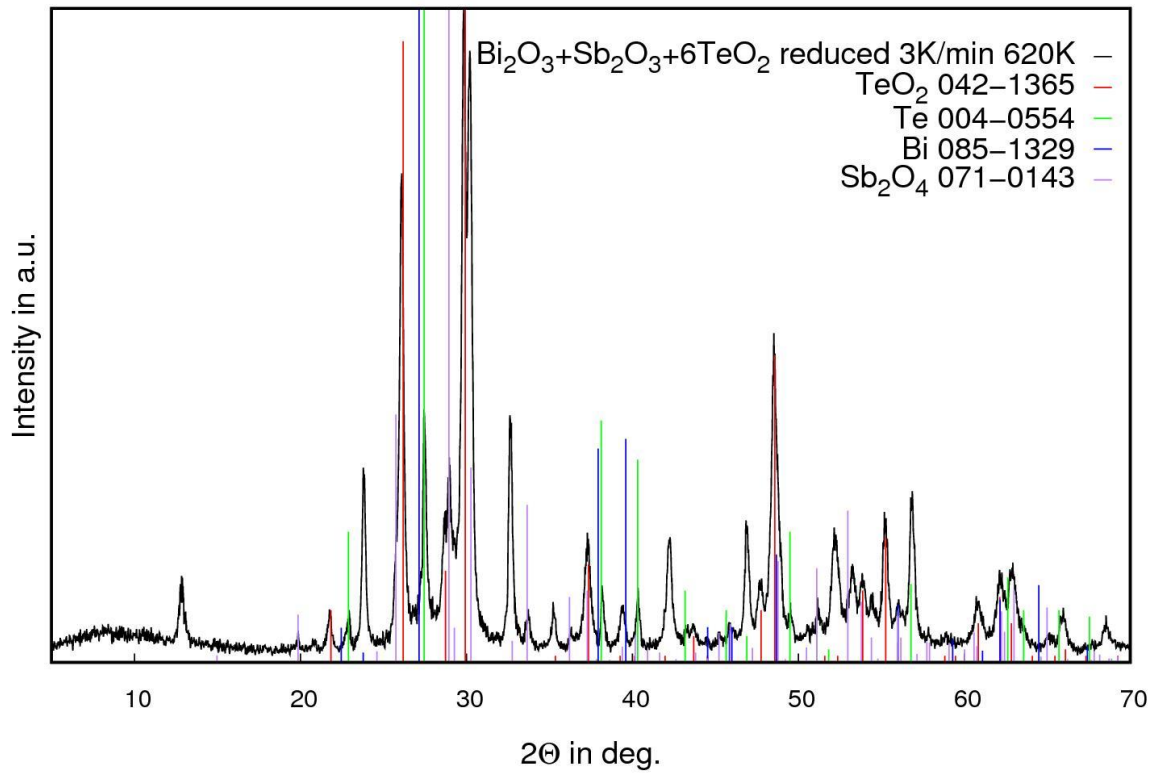

Fig. S6.2. The diffraction pattern of the Bi_2O_3+ Sb_2O_3+6TeO_2 powder reduced in hydrogen up to 620 K with a 3 K/min heating rate with reference patterns.

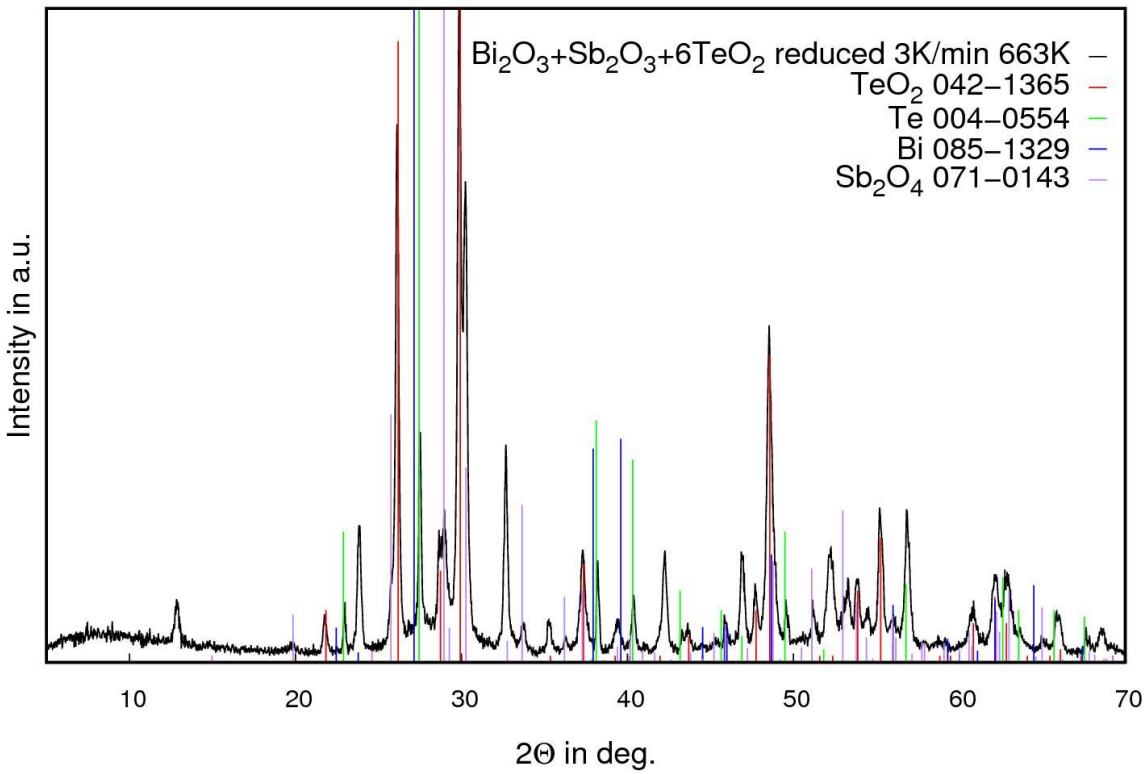

Fig. S6.3. Diffraction pattern of the Bi_2O_3+ Sb_2O_3+$6TeO_2$ powder reduced in hydrogen up to 663 K with a 3 K/min heating rate with reference patterns.

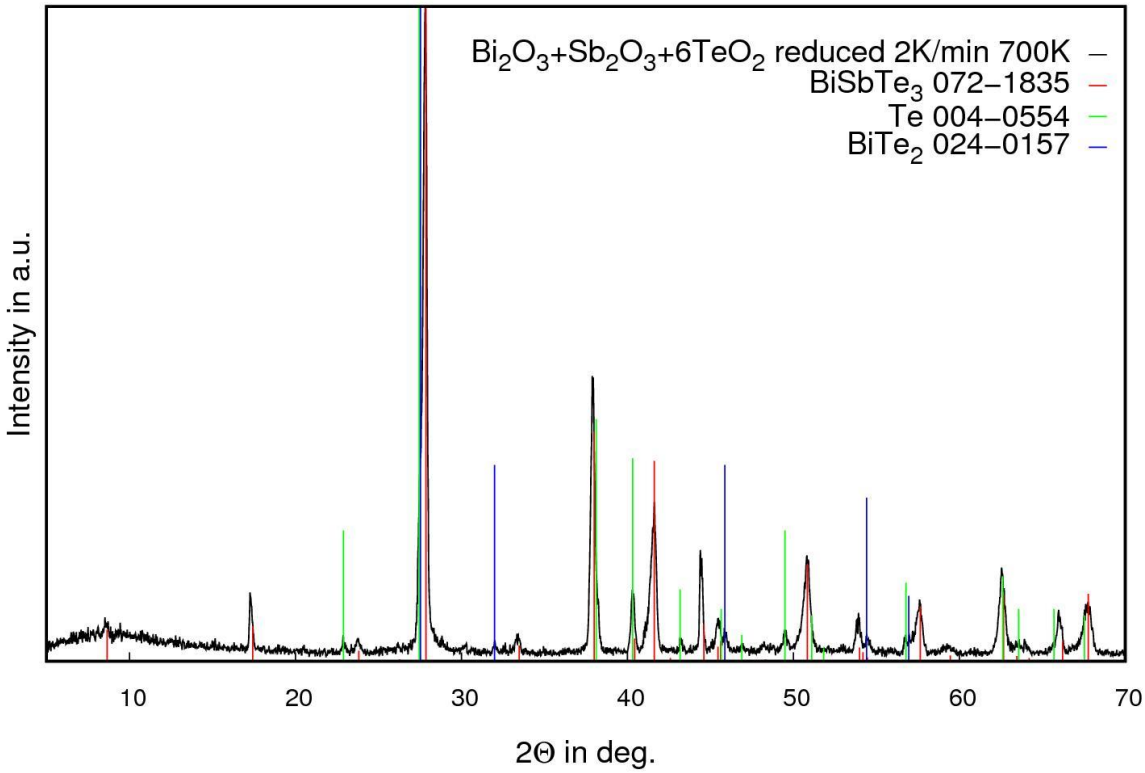

Fig. S6.4. Diffraction pattern of the Bi_2O_3+ Sb_2O_3+$6TeO_2$ powder reduced in hydrogen up to 700 K with a 2 K/min heating rate with reference patterns.

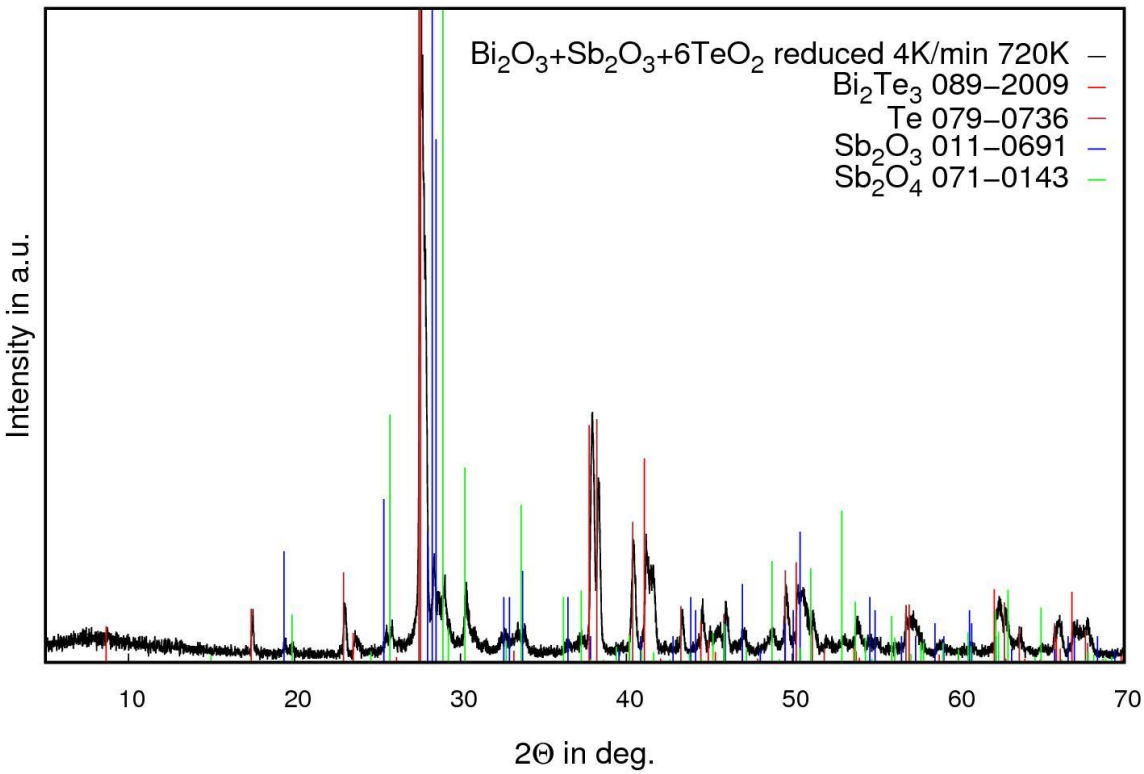

Fig. S6.5. Diffraction pattern of the Bi_2O_3+Sb_2O_3+6TeO_2 powder reduced in hydrogen up to 720 K with a 4 K/min heating rate with reference patterns.

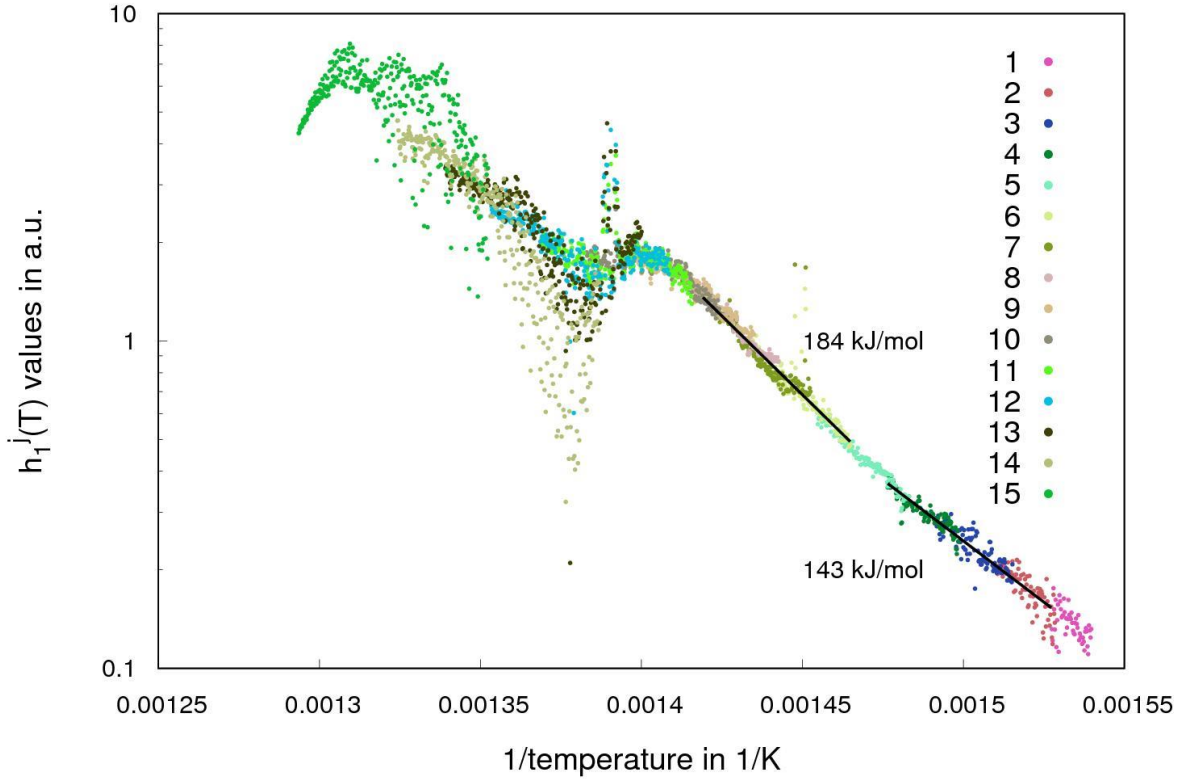

Fig. S6.6. Thermal function $h(T)$ calculated with the NPK analysis of the reduction of Bi_2O_3+Sb_2O_3+6TeO_2. Values in the key stand for j indices of vectors $\mathbf{v_1}^j$.

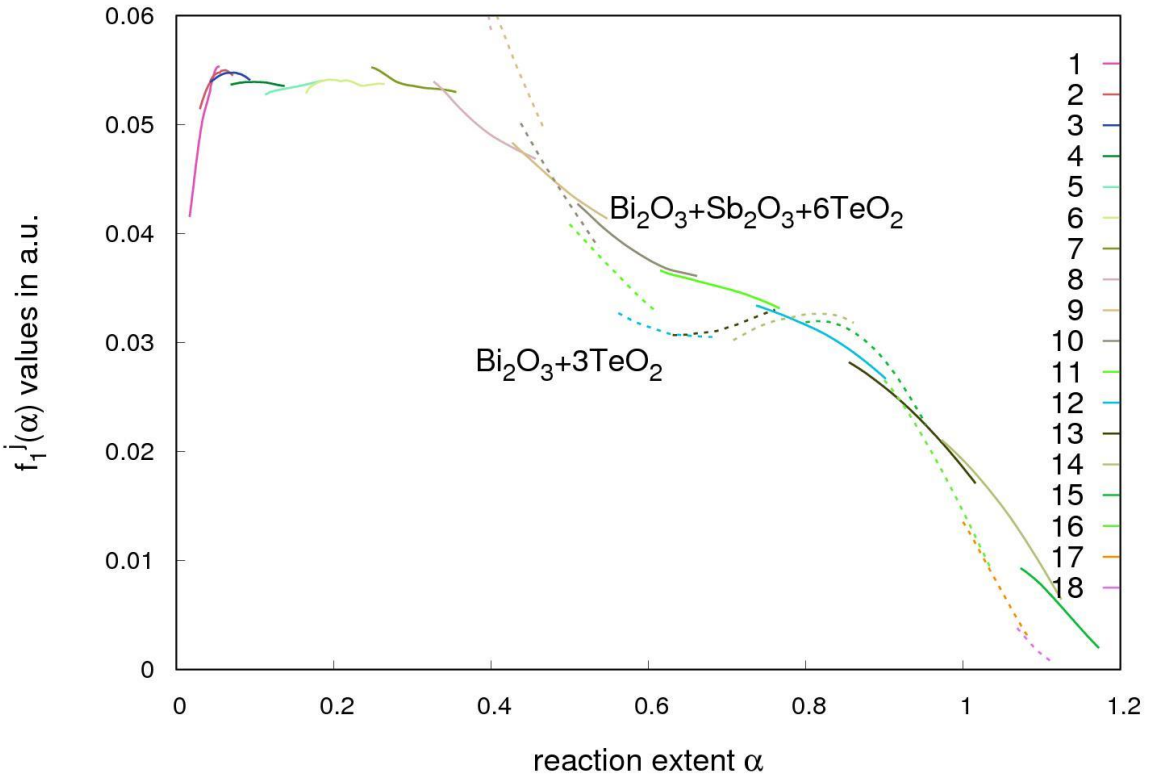

Fig. S6.7. Conversion function $f(\alpha)$ calculated with the NPK analysis of the reduction of Bi_2O_3+3TeO_2 scaled by a factor of 3(dashed line) and Bi_2O_3+Sb_2O_3+6TeO_2 (solid line). Values in the key stand for j indices of vectors $\mathbf{u_1}^j$.

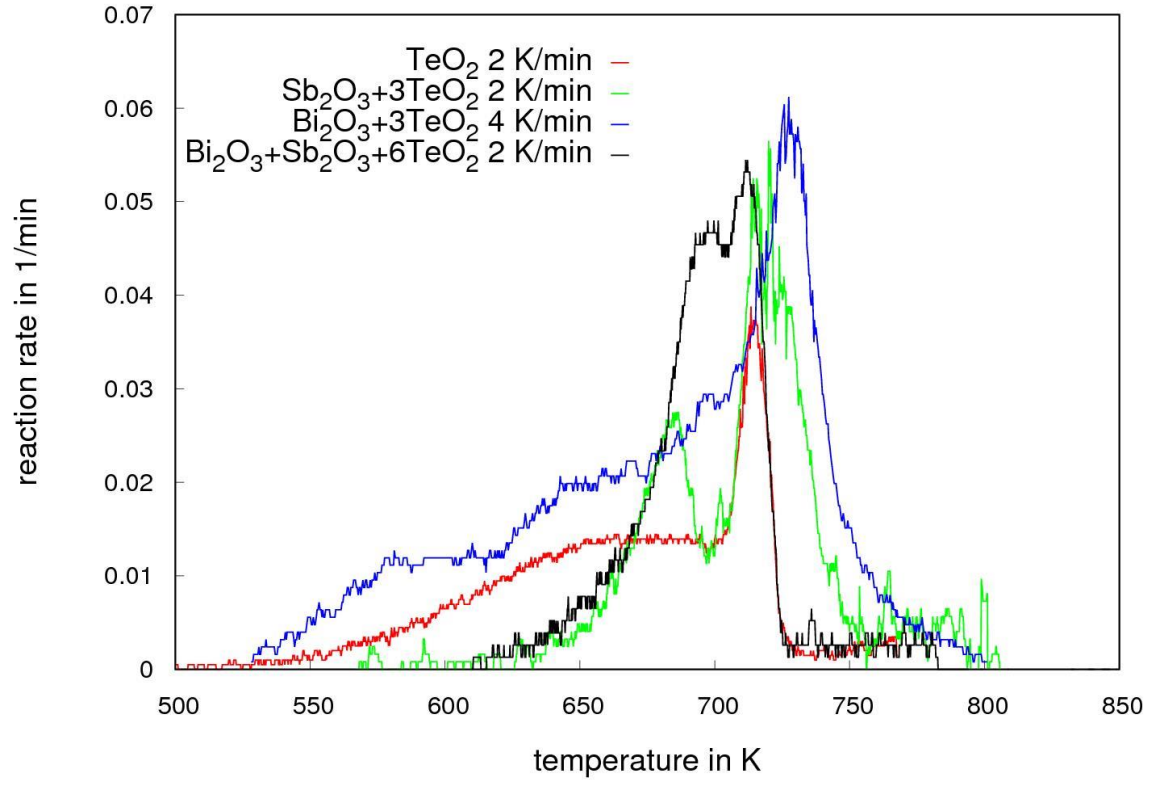

Fig. S6.8. Comparison of the reaction rate dependence on temperature for different oxide powders. In the case of the Bi_2O_3+3TeO_2 powder, the 4 K/min results are given, because in the 2 K/min run the self-heating was not observed (another mechanism of the reaction was observed).